Full length article

Phosphorus and transition metal co-segregation in ferritic iron grain boundaries and its effects on cohesion

Han Lin Mai [a], Xiang-Yuan Cui [a], Daniel Scheiber [b], Lorenz Romaner [c], Simon P. Ringer [a],*

[a] *School of Aerospace, Mechanical and Mechatronic Engineering & Australian Centre for Microscopy and Microanalysis, Faculty of Engineering, The University of Sydney, 2006 New South Wales, Australia*
[b] *Materials Center Leoben Forschung GmbH, Roseggerstraße 12, 8700 Leoben, Austria*
[c] *Department of Materials Science, University of Leoben, Franz-Josefstraße 18, 8700 Leoben, Austria*

ARTICLE INFO

ABSTRACT

The phenomenological interplay in the segregation of phosphorus (P) and transition metal (TM) elements at grain boundaries (GBs) in steels has long been suspected to be the main contributor to temper embrittlement. However, many of the details remain unclear. Here, we investigate the segregation, co-segregation and cohesion effects of TMs (Co, Cr, Cu, Mn, Mo, Ni, Nb, Ti, V, W) along with P in various ferritic iron (α-Fe) GBs utilising density functional theory and simulations of kinetics. Our findings demonstrate that P is unlikely to cause intergranular fracture via weakened interfacial bonding when segregated by itself. Nevertheless, the stronger segregation binding of P compared to TMs can explain the ubiquitous presence of P segregated at GBs. We find that most P-TM interactions at ferritic GBs are repulsive and differ significantly from the corresponding interactions in the bulk. Due to the repulsive interactions and strong segregation binding of P, the enrichment of P over time at GBs leads to the depletion of prior-segregated cohesion-enhancing solutes at general GBs. Additionally, certain P-TM co-segregation combinations that are cohesion-lowering are energetically favoured at such GBs. We posit these mechanisms act in tandem as critical causalities of P-induced temper embrittlement in alloyed steels. Finally, we reveal a contradiction in the predicted cohesion effects of segregated P calculated in the Rice–Thomson–Wang theory of interfacial embrittlement compared to that as assessed by chemical bonding strength, calculated in the DDEC6 bond-order framework. These findings have important implications for GB engineering for interfacial cohesion.

1. Introduction

Temper embrittlement is one of the oldest unresolved problems in the metallurgy of steels. The phenomenon is characterised by a brittle failure mode that occurs via intergranular fracture after an alloy steel undergoes prolonged exposure to temperatures in the range of 400–600 °C [1]. Temper embrittlement can cause the sudden, unexpected catastrophic failure of steel alloys [2]. It is well-accepted that grain boundary (GB) segregation of impurities and alloying additions play a central role in temper embrittlement [1,3–5]. This segregation can alter the cohesion of the GBs through chemical effects, allowing for them to be strengthened or weakened, depending on the specific elements segregated. As a result, extensive research efforts, experimental and theoretical, have been devoted to studying the effects of segregation of varying alloying additions and impurities on GB cohesion in steels. Despite this extensive body of research, there remains significant uncertainty regarding the specific mechanisms by which temper embrittlement occurs [6].

One of the most well-studied impurities with regard to temper embrittlement in steels is P, since it has long been suspected to be the main culprit behind the phenomenon. Pioneering experimental efforts observed the consistent presence of P on intergranularly-fractured surfaces of temper-embrittled steels [7–14], leading to the conclusion that temper embrittlement could be mostly attributed to P-segregation to GBs. However, its exact role in temper embrittlement remains unclear [6].

Importantly, temper embrittlement manifests prominently in structural alloy steels, and does not occur in pure unalloyed steels [1]. Transition metals (TMs) are one of the most important groups of alloying elements for steels, employed for purposes such as grain size stabilisation [e.g. Mn [15]], imparting corrosion resistance [e.g. Cr [16]] or their potential to drive clustering-induced strengthening [e.g. Nb [17], Ti [18]]. As a result, significant research has been devoted to investigating the role that alloying TMs play in temper embrittlement.

---

* Corresponding author.
  E-mail address: simon.ringer@sydney.edu.au (S.P. Ringer).

Particular focus was placed on Mn, Ni, and Cr, since they are common alloying elements found in structural alloys known to be susceptible to temper embrittlement. Similarly, Mo has received attention, since empirically it is known to alleviate temper embrittlement [1]. This, combined with earlier investigations on the role of P, led to the formation of Guttmann's theory of co-segregation [19]. The theory attributed temper embrittlement in steels to the synergistic co-segregation of P-TM solute couples to GBs. It attributed the lack of embrittlement in alloys containing so-called embrittlement-reducing solutes such as Mo to attractive solute interactions in the bulk which prevented the segregation of P to the GBs [12,14,19–22]. However, this theory was not supported by later experimental results [23–26]. Uncertainty surrounding the validity of the phenomenology of embrittlement proposed by Guttmann's theory is exacerbated by the lack of data detailing these P-TM solute–solute interactions at GBs.

Beginning in the 1990s, a body of simulation studies mostly led by Olson and co-workers investigated the effects of P segregation and P-TM co-segregation on the cohesion of Fe GBs [27–36]. However, these works almost exclusively considered only the $\Sigma 3[110](1\bar{1}1)$ GB. Furthermore, P was assumed to occupy an interstitial position at the GB interface and few specific interaction constellations between P-TM were studied. Recent research has shown that P often occupies substitutional positions in various ferritic Fe GBs [37], corroborating the results in an earlier work by Yamaguchi et al. [34], which determined a preference for the substitutional site in the $\Sigma 3[110](1\bar{1}1)$ GB. The story of the P-induced temper embrittlement is further complicated by results such as those generated by Messmer and Briant, who suggested from the results of chemical bonding analysis that P in isolation is only a weak embrittler of GB cohesion [38,39]. They proposed that temper embrittlement could instead be attributed to enhanced embrittling potency enacted by co-segregated P-X solute couples. Ab-initio calculations in the Rice–Thomson–Wang framework by Yamaguchi et al. have confirmed that elemental P is only a weak embrittler of a ferritic Fe GB [34]. Since GB character is known to be critical in controlling both the tendency, or otherwise, for solute segregation, their interactions, and the induced cohesion effects [40–42], a wider range of GB structures must be studied before definitive conclusions may be drawn on the effect of elemental P on GB cohesion.

No simulation studies have systematically studied the co-segregation interaction energetics of P with common alloying TMs at GBs. While substitutional P-X solute–solute interactions have been thoroughly studied in bulk ferritic Fe by Gorbatov et al. in [43], solute interaction behaviours can be drastically different at GBs. These differences can in turn affect co-segregation energetics [42,44]. Furthermore, it has been shown that co-segregation interactions of solute pairs can vary significantly depending on the GB character [42]. This also limits the generality of the conclusions that may be drawn from these previous works. These lingering uncertainties leave the issue of how P may interact with TMs at GBs unclear. Therefore, the assumed interactions in Guttmann's theory remain untested from a simulation standpoint. Furthermore, it has been shown that the effects of segregated TM solutes on GB cohesion can change as a function of GB character [42]. Critically, whether synergistic co-segregation of P-TM solute pairs actually occurs across archetype boundaries in alloy steels remains unclear. It is also unclear how this co-segregation might affect the local GB cohesion.

As an example of the confusion in this field, the role of Mn in temper embrittlement is unclear. Some studies suggest that intergranular failure may be directly attributed to GB interfacial embrittlement occurring due to Mn segregation [45–47]. Alternatively, others claim that it is the very high strength of the matrix in relation to grain boundaries that is to blame for the often observed intergranular fracture [48]. While some attribute embrittlement to Mn segregation, others claim that P–Mn co-segregation [49] may be responsible for embrittlement. This is further complicated by results from DFT studies, revealing that the cohesion effects of segregated Mn, as computed in the Rice–Thomson–Wang

framework, have a negligible effect on the cohesion of a $\Sigma 3[110](1\bar{1}1)$ Fe GB [50,51], and that Mn segregation, may, in fact, be beneficial to cohesion in other boundaries [42,52]. A similarly confusing story exists for the Mo–P, Cr–P and Ni–P couples and their effects on temper embrittlement [6,23].

One of the longstanding issues in the study of GB cohesion is the use of differing techniques for assessing the effects of segregated solutes. Here, we describe two of the main approaches. The first involves the calculation of an "embrittling potency" or "strengthening energy" in the Rice–Thomson–Wang thermodynamic theory of interfacial embrittlement [53,54]. Henceforth, we refer to this simply as the "cohesion effect", which may be negative (embrittling) or positive (strengthening). A second approach to assess the cohesion effect of a segregated solute utilises a direct analysis of the change in the atomic chemical bonding states at the interface to assess the cohesion effect of a segregated solute [39]. Most recent studies favour the former method for assessing the effects of segregated solutes on GB cohesion, due to the ease of comparison and reproducibility of single numerical values such as the work of separation, compared to chemical bonding analysis. On the other hand, recent advances in techniques for the analysis of chemical bonds [55] allow singular values to be prescribed in the quantitative description of the cohesion effects of segregated solutes on specified cleavage planes along GBs [42]. Furthermore, some have criticised the fundamental thermodynamic assumptions upon which the widely used Rice–Thomson–Wang framework is built upon, instead favouring a chemical bonding perspective for assessing GB cohesion [56,57]. This issue remains unresolved since until now, very few papers have directly quantified the strength of chemical bonding at GB interfaces to compare with the corresponding work of separation quantities generated in the Rice–Thomson–Wang framework. Thus, a comparison of the results generated in both frameworks is crucial to advance our fundamental understanding of the effects of segregation on interfacial cohesion.

A deeper understanding of the role of P in the temper embrittlement of steels requires a more comprehensive understanding of its segregation and co-segregation phenomenology, and the resultant induced cohesion effects across a range of GB characters. Here, we utilised density functional theory (DFT) to comprehensively investigate the segregation and induced cohesion effects of the common alloying TMs, Co, Cr, Cu, Mn, Mo, Ni, Nb, Ti, V, W, and substitutional P atoms, in various model bcc-Fe GBs. The co-segregation of all P-TM pair cases was considered, the solute–solute interactions at the GBs quantified, and their resultant effects on cohesion analysed. We specifically investigated whether co-segregated P-TM couples can enable a decohesive effect on GB cohesion that is not evident from their individual behaviours. We compared the results generated for cohesion assessment in both the Rice–Thomson–Wang framework [53,54] and the DDEC6-based chemical bond-order framework [55]. The role of heat treatment and site competition on solute coverage at the GB in all Fe–P–TM ternary alloys are considered using thermo-kinetic simulations.

2. Methodology

We performed first principles calculations based on DFT using the projector augmented wave (PAW) method [58] as implemented in the Vienna Ab-initio Simulation Package (VASP) [59,60]. Spin polarisation was accounted for in all calculations performed in this study. We utilised the generalised gradient approximation (GGA) via the Perdew–Burke–Ernzerhof (PBE) functional [61]. The Brillouin-zone integrations for all GBs employed Γ-centred **k**-point meshes, with an energy cut-off of 400 eV for the plane wave basis set. A first–order Methfessel–Paxton scheme with a smearing width of 0.2 eV was adopted for all calculations. When forces on each atom were relaxed, the criterion for relaxation convergence was set to forces below 0.01 eV/Å, and the criterion for total energy convergence in the electronic minimisation iterations was set to 1×10^{-5} eV. We utilised **k**-point meshes of $6 \times 3 \times 1$, $6 \times 6 \times 1$, $6 \times 4 \times 1$ and $6 \times 6 \times 1$ for the $\Sigma 3(1\bar{1}1)$, $\Sigma 3(1\bar{1}2)$, $\Sigma 9(2\bar{2}1)$ and
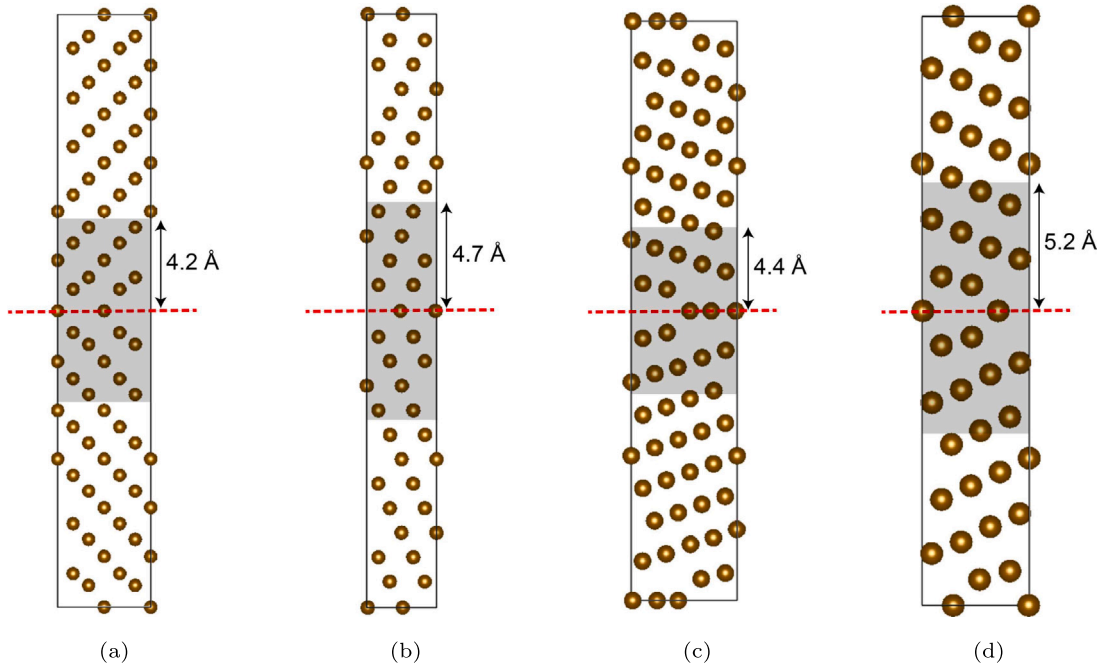
Fig. 1. The atomic structures of the four characteristic model GBs studied: the 1(a) $\Sigma3[110](1\bar{1}1)$, 1(b) $\Sigma3[110](1\bar{1}2)$, 1(c) $\Sigma9[110](2\bar{2}1)$ and the 1(d) $\Sigma11[110](3\bar{3}2)$ GBs, respectively. The GB interface planes are highlighted by the dashed red lines. The shaded ranges indicate the range of studied sites for segregation and co-segregation. The cells with vacuum are plotted in Supplementary Fig. S1. The dimensions of these cells are given in Table 1.

$\Sigma11(3\bar{3}2)$ GBs, respectively. Our selections of the exchange–correlation functional, **k**-point meshes, plane wave energy cut-off and grain lengths were checked with convergence tests. The convergence tests for these GBs were previously conducted and presented in our prior published work [42].

2.1. Grain boundary structures

In this study, four model symmetric tilt GBs, the $\Sigma3[110](1\bar{1}1)$, $\Sigma3[110](1\bar{1}2)$, $\Sigma9[110](2\bar{2}1)$ and $\Sigma11[110](3\bar{3}2)$ were investigated. Their atomic structures are presented in Fig. 1. These four GBs possess underlying structural features that represent various archetypes. These span the "twin" type - $\Sigma3[110](1\bar{1}2)$ and typical "high-angle tilt coincident site lattice" - $\Sigma3[110](1\bar{1}1)$, $\Sigma11[110](3\bar{3}2)$. The $\Sigma9[110](2\bar{2}1)$ GB possesses an edge-dislocation core–like structure at the interface, and as such, it has the characteristics of a low-angle tilt GB [62]. Herein, for brevity, they are referred to as $\Sigma3(1\bar{1}2)$, $\Sigma3(1\bar{1}1)$, $\Sigma11(3\bar{3}2)$ and $\Sigma9(2\bar{2}1)$, respectively. These GBs are formed from a range of typical structural units [62–64], allowing for an examination of segregation phenomena across a wide range of local atomic environments at the interface. Note that symmetric tilt GBs occur more frequently about the $\langle110\rangle$ axis in polycrystalline bcc-Fe than about others [62].

In our construction of these GBs, atoms that were less than 0.7 times the bulk lattice vector apart in distance were merged to become a single site, as to be consistent with the structures in Ref. [62]. This affected the $\Sigma9(2\bar{2}1)$ and $\Sigma11(3\bar{3}2)$ GBs. We constructed the GBs via the python package Atomic Simulation Environment [65]. Our cells were all orthorhombic, with the exception of the $\Sigma9(2\bar{2}1)$, which was rhombic. The cells were constructed utilising the converged lattice vector as found in the functional testing, $a_0 = 2.832$ Å. In the calculations of GB energies/excess volumes, which involve cells without a vacuum slab, an optimisation of the "c" cell length (perpendicular to the GB plane) of the constructed supercell was performed while the "a" and "b" (the in GB-plane directions) dimensions were kept fixed. A vacuum slab was included in all other calculations, and cell relaxations (shape/volume) were not performed. The vacuum slab sizing was >11 Å in all non-cleaved cells in order to ensure the exclusion of spurious

surface–surface interactions. The relaxed GB structures in the vacuum cells are available as POSCAR files in the S.I. Atomic relaxations were performed in all calculations except those in the rigid-separation schemes.

The grain boundary energies and excess volumes for each of the four model GBs in this study are presented in Table 1. Both are standard quantities for characterising GBs [66,67]. For the details of the methodology used to calculate these quantities, we refer readers to our previous work [42], which employed the same methodology on the same grain boundaries, for brevity purposes.

We explicitly investigated the gamma-shift energy surface investigating the microstructural degrees of freedom for atoms in all four GBs [Supplemental Table S1]. The shifts were conducted in a grid-search manner along the "a" and "b" cell directions ranging 0.0–0.5 inclusive (due to symmetrical redundancy) in fractional coordinates, with step width 0.1, which resulted in 36 calculations conducted for each GB. The shifts were conducted between the GB plane and the nearest parallel plane of atoms. We did not allow atoms to relax in one half of the cell (excluding the middle plane), and only allow the relaxation of atoms in the "z" direction for the other half. There were no gamma-shifted structures that were energetically favoured in comparison to the as-built cell (a-shift = 0.0, b-shift = 0.0). As such, we utilised the as-built symmetrical GBs as the base model GBs for the subsequent segregation and co-segregation studies. It cannot be excluded, however, that a shift may occur with solute segregation in select cases. A detailed investigation of such effects is beyond the scope of this work.

2.2. Segregation

2.2.1. Segregation energy

Segregation energies represent the energy difference of a solute being situated at the GB compared to the bulk. The segregation energy (E_{seg}) of a substitutional solute X at any site is calculated with the following:

$$E_{seg}(X) = E_{GB}\left[(n-1)Fe, X\right] - E_{GB} - \left[E_{Bulk}\left[(m-1)Fe, X\right] - E_{Bulk}\right] \quad (1)$$

Where $E_{GB}\left[(n-1)Fe, X\right]$ is the total energy of a GB structure with n atoms containing a substitutional solute X, E_{GB} is the total energy of the
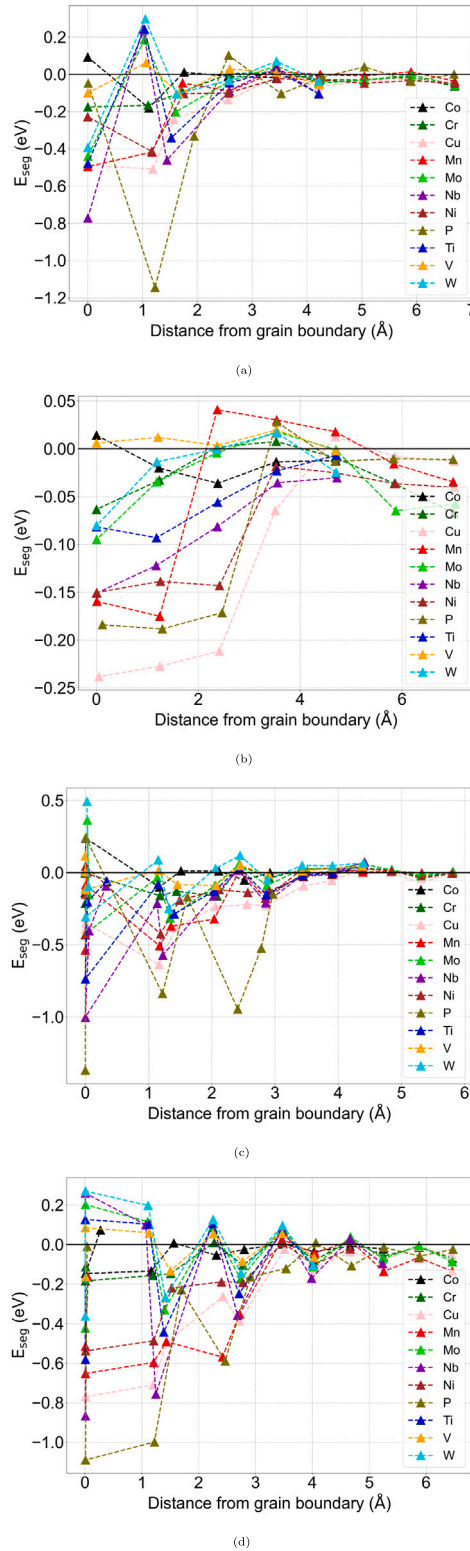
(a)

(b)

(c)

(d)

Fig. 2. The segregation energy profiles of all solutes across the tested substitutional sites are plotted against their distance from the GB interface. The profiles are plotted for the 2(a) $\Sigma3[110](1\bar{1}1)$, 2(b) $\Sigma3[110](1\bar{1}2)$, 2(c) $\Sigma9[110](2\bar{2}1)$ and 2(d) $\Sigma11[110](3\bar{3}2)$ GBs. The data is tabulated in Supplementary Tables S6–S10. in the S.I.

pure GB containing n Fe atoms, $E_{Bulk}\left[(m-1)Fe, X\right]$ is the total energy of a bulk slab with m atoms containing a substitutional solute X, and

E_{Bulk} is the energy of that bulk cell in its pure form, containing m Fe atoms. The respective m and n for each case are presented in Table 1. Here we used slab cells that possessed the same dimensions as the GB to minimise the numerical errors associated with **k**-point sampling errors that occur due to different cell sizings [68].

Segregation energies for an interstitial solute at the GB that prefers substitutional sites in the bulk, are instead calculated with:

$$E_{seg}(Y) = E_{GB}\left[(n)Fe, X\right] - E_{GB} - \left[E_{Bulk}\left[(m-1)Fe, X\right] - E_{Bulk} + E_{bulk}/m\right] \quad (2)$$

Since an additional Fe atom is present in the GB with an interstitial solute compared to a pure GB, an extra term for the energy of one additional bulk Fe atom (E_{bulk}/m) is necessary to normalise the energies in the GB part of the equation.

Negative values of E_{seg} indicate that a solute prefers to be situated at the GB compared to the bulk, i.e. *segregation*, with more negative values indicating stronger segregation tendencies. Positive values indicate anti-segregation, where a solute prefers the bulk to the GB environment. Importantly, these segregation energies may be used to determine real site-occupancy probabilities at the GB at some temperature and overall bulk solute concentration, by acting as inputs into the frameworks of various thermodynamic theories, e.g. those formulated by Langmuir-McLean [69] or White-Coghlan [70].

2.3. Solute–solute configurations

Here, we investigated the co-segregation of P in the presence of the tested TMs. We studied two cases. The first involves P as the prior segregated atom, and a secondary segregating atom was permuted around the GB structure, herein referred to as P-X. The second involved the reverse segregation order of the solutes in the first case, herein termed X-P. In each case, solute 1 was placed in the most energetically favourable site at the pure GB and is fixed in that site, and solute 2 was permuted around the GB decorated with solute 1, and vice versa. This approach is similar to that presented in our previous study studying TM co-segregation in the same GBs [42] and that employed by others in other systems [71,72]. This effectively considered both the P-X and X-P co-segregation sequences, capturing both scenarios. In this process, we permuted the secondary atom across all sites that were within some minimum threshold distance away from the interface [Fig. 1].

Note that this method ostensibly neglects the possibility that the most energetically favourable configuration could have solutes occupying a site-combination that does not involve either solute at their most energetically favourable site in the pure-GB. However, many solute–solute interactions at the GB are generally of small magnitude, and where significant, are mostly repulsive in nature [42]. We also note the sharp decrease in the magnitude of strength of segregation binding beyond the most favourable site, Fig. 2. These combined factors of energetically repulsive solute–solute interactions with small segregation tendencies at other sites should render this possibility highly unlikely. Thus, it is reasonable to assume that our study accurately captures most of, if not all, of the minimum energy pair-configurations at the GB.

2.3.1. Incremental segregation energy

The *incremental* segregation energy (E_{seg}^{inc}) is used to measure the likelihood of a second solute atom Y segregating to a GB that has been prior decorated with a segregated solute X. We calculated this quantity using:

$$E_{seg}^{inc} = E_{GB}\left[(n-2)Fe, X, Y\right] - E_{GB}\left[(n-1)Fe, X\right] - \left[E_{Bulk}\left[(m-1)Fe, Y\right] - E_{Bulk}\right]$$

$$(3)$$

Where $E_{GB}\left[(n-2)Fe, X, Y\right]$ is the total energy of a cell containing solute atoms X, Y in substitutional positions.

2.3.2. Total segregation energy

The *total* segregation energy can be used to assess the likelihood of a pairing of solute atoms segregating to a particular grain boundary in absolute terms. We calculated this quantity using:

$$E_{seg}^{total} = E_{GB}\left[(n-2)Fe, X, Y\right] - E_{GB}$$
$$- \left[E_{Bulk}\left[(m-1)Fe, X\right] + E_{Bulk}\left[(m-1)Fe, Y\right] - 2E_{Bulk}\right] \quad (4)$$

2.3.3. Interaction energy

The interaction energy is used in this study to quantify the magnitude and type of interaction that occurs between solute X and solute Y at the GB. It was calculated by:

$$E_{int} = E_{GB}\left[(n-2)Fe, X_i, Y_j\right] - E_{GB}\left[(n-1)Fe, X_i\right] - E_{GB}\left[(n-1)Fe, Y_j\right] + E_{GB} \quad (5)$$

Where $E_{GB}\left[(n-2)Fe, X_i, Y_j\right]$ is the total energy of a GB containing substitutional solutes of element X and Y at sites i and j, respectively. Positive values indicate that this interaction is repulsive (i.e. energetically unfavourable), whereas negative values indicate that this interaction is attractive.

2.4. Cohesion

2.4.1. Work of separation (rigid/relaxed) - W_{sep}

The Rice–Thomson–Wang model of thermodynamic interfacial embrittlement identifies the work of separation (W_{sep}) as a key quantity in the determination of fracture [53,54]. The work of separation of a GB may be expressed as a function of the cells containing a cleaved GB (i.e. with two free surfaces, separated at a specified cleavage plane), denoted by E_{GB-sep}, and a GB only. The cleavage planes tested were parallel to the GB plane, and in the case of a pure GB with no segregants, this is usually equivalent to cleaving at the GB plane. So:

$$W_{sep} = (E_{GB-sep} - E_{GB})/A. \quad (6)$$

Note that the work of separation may also be computed as a function of the free surface energy (γ_{FS}). The free surface energy may be computed via:

$$\gamma_{FS} = (E_{bulk} - N_{bulk}/N_{slab} \times E_{slab})/(2A) \quad (7)$$

Where E_{slab} is the energy of a slab cell with two free surfaces, each with area A. The work of separation may also be calculated using: $W_{sep} = 2\gamma_{FS} - \gamma_{GB}$.

Two methods were used to determine the work of separation in this study. These were related to the mode of separation employed at a chosen cleavage plane with respect to the relaxation of the surfaces. In the first method, relaxations of the surfaces formed by the cleaving of the grains were not performed. The quantity yielded by this method is the *rigid* work of separation, W_{sep}^{RGS}. This quantity is also known as the fracture energy. The second method, which allowed for surface relaxations in the cleaved grain cells, is the standard for determining the work of separation. This second quantity is denoted as W_{sep}. We extensively tested all cleavage planes parallel to the GB plane [42,73,74]. Diagrams depicting the chosen cleavage planes in each GB are presented in Supplementary Fig. S11. We used the *rigid* work of separation to determine the favourable cleavage plane, which is the plane that minimises the W_{sep}^{RGS} required to cleave the grains. The cleaved structure at the plane that yielded the minimum W_{sep}^{RGS} was then used to calculate the *relaxed* W_{sep}. Note that it is prudent to take the lowest bound of GB cohesion for engineering purposes, and as such only the smallest W_{sep}^{RGS} values computed across all cleavage planes are presented in this study.

Here we note Fernandez et al. have proposed a statistical-ensemble type approach for assessing GB cohesion when utilising Rice–Thomson–Wang theory for assessing fracture properties [75]. In their work, they computed GB fracture tendencies (the works of separation) across all cleavage planes across all possible segregation positions of a solute.

Here, we only consider the cleavage plane possibilities at the most likely segregation site for a solute. We do not employ their approach here due to the additional computational cost required for these sets of calculations, which are multiplied by the permutational nature of our co-segregation study. As such, these computations are left for future work.

2.4.2. Sutton's ratio - R

Sutton's ratio [76] (R) is a measure of the likelihood of the intergranular fracture occurring compared to transgranular fracture in brittle failure modes. Values of R close to or greater than 1 indicate that transgranular fracture is preferred, whereas lower values indicate a preference for intergranular fracture modes. It is calculated in the manner:

$$R = \frac{W_{sep}}{2\gamma_{FS}^{PCP}} \quad (8)$$

Where γ_{FS}^{PCP} is the free surface energy of the preferred cleavage plane in the bulk metal. In this study, we used the calculated free surface energy of the Fe (100) BCC surface of 2.50 J/m^2 for the quantity γ_{FS}^{PCP}, which has been suggested for BCC crystals in [77].

2.4.3. Cohesion effect (Rice–Thomson–Wang framework) - η

The cohesion effect (η) of a solute may be quantified in the Rice–Thomson–Wang framework by taking the difference between the works of separation in the structures with and without the segregated solutes. As mentioned, this term is often referred to as the embrittling potency, or strengthening energy. In this work, it is referred to as the cohesion effect and was calculated by:

$$\eta = W_{sep}^{seg} - W_{sep}^{0} \quad (9)$$

Where W_{sep}^{0} and W_{sep}^{seg} are the works of separation of the pure GB and the GB with segregated atoms, respectively. Note that it is prudent to assess the cohesion difference as the difference in the strength of the interface at the weakest cleavage plane in the pure and segregated GBs. As such, the smallest values of W_{sep}^{0} and W_{sep}^{seg} across all cleavage planes were used in the calculation of η. Negative values of η indicate that a solute possesses an embrittling (decohesive) effect for GB cohesion, whereas positive values indicate a cohesion enhancing effect of the solute on the GB.

2.4.4. Area-normalised summed bond-orders (ANSBO)

In this study, we have computed the electron density-derived bond orders in the GBs utilising the DDEC6 framework [55]. We used a bonding-based cohesion quantity, the *Area-Normalised Summed Bond Orders* (ANSBO) in order to quantify the interface bonding strength [42]. The formulation of ANSBO is analogous to the concept of the work of separation in the Rice–Thomson–Wang framework. Both formulations generate a single quantity for interfacial cohesion strength at any specified cleavage plane, which allows them to be compared directly. In our calculation of the ANSBO for each structure, we identified all the bonds that passed through each of the studied cleavage planes. The sum of all bond orders of the bonds passing through a specific cleavage plane was calculated. For bonds extending into neighbouring cell images, we halved the corresponding bond order values in the calculation of ANSBO. Let us take the example of the quantification of the strength of bonding at a GB across any specific fracture path in the "x–y" plane at height "z". Mathematically:

$$\sum_{\substack{frac \\ path}} BO = \sum_{i,j}^{i \neq j} BO[X_i, X_j] + \frac{1}{2} \sum_{k,l}^{k \neq l} BO[X_k, X_l] \quad (10)$$

$$where \ X_1(z) < z_{CP} < X_2(z)$$

$$ANSBO = \sum_{\substack{frac \\ path}} BO/A \quad (11)$$

Where X_i, X_j, X_k, X_l are the atoms that are electronically bonded in sites i, j, k, l respectively, and X_1, X_2 represent the i, j and the k, l pairings in any order. X_i and X_j atoms reside entirely within the supercell created (i.e. bonds exist wholly within the cell), whereas X_k and X_l represent atom pairs where only one of X_k and X_l resides in the cell (i.e. possess bonds passing outside of the original cell into a neighbouring image). z_{CP} is the z coordinate of the cleavage plane. Larger values of ANSBO indicate greater strength of interfacial cohesion. The values presented are the minimum calculated values of the ANSBO in each interface across all studied cleavage planes.

2.4.5. Cohesion effect - η_{ANSBO}

In this study, the strength of interfacial cohesion was assessed on a chemical-bonding basis, via the ANSBO quantity described previously. It follows that the effect of a segregated atom on interfacial cohesion may be quantified by taking the difference between the ANSBOs of the pure GB and the segregated GB. We denote this quantity as η_{ANSBO}. As prior, consistent with W_{sep} and η in the Rice–Thomson–Wang framework, it was the smallest value of ANSBO in the pure and segregated GBs calculated across all cleavage planes that was utilised in our calculation of η_{ANSBO}. Thus, the lowest ANSBO value found in the pure and segregated structures were used as the representative values in the calculation of η_{ANSBO}:

$$\eta_{ANSBO} = ANSBO_{seg} - ANSBO_{pure} \tag{12}$$

Where η_{ANSBO} is the cohesion change attributed to the segregated solute, and $ANSBO_{pure}$, $ANSBO_{seg}$ the minimum calculated values of ANSBO across all cleavage planes in the pure GB and segregated GB cases, respectively. As with the calculated values of η in the Rice–Thomson–Wang framework, positive (negative) values of η_{ANSBO} indicate that the strength of interfacial cohesion is increased (reduced) by the presence of the segregated solute.

2.4.6. Changes in bonding state

To further investigate the bonding from a more granular perspective, it was necessary to perform a direct analysis of the bonding of the segregated solute atoms at the GB. This was achieved by comparing the summed DDEC6 bond orders of atoms in the segregated and pure GBs, respectively. Intuitively, this may be described as a direct comparison of the changes in the bonding that occurs at a GB when a segregated atom replaces a Fe atom at the GB. We quantified these changes by taking the difference in the summed bond orders of the site in the pure and segregated cases, respectively. This allowed us to determine how the bonding is changed in the immediate vicinity of the segregated atom, compared to if the site was occupied by the host-lattice atom (Fe). This quantity was calculated by taking the difference in summed bond orders of the solute atom and the Fe atom that it replaced:

$$\Delta SBO(N) = \sum BO_{seg}(N) - \sum BO_{pure}(N) \tag{13}$$

Where $\Delta SBO(N)$ is the attributable change in the bond orders that occur due to the replacement of a host lattice atom with solute atom N, and $\sum BO_{seg}(N)$, $\sum BO_{pure}(N)$ are the summed bond orders of the solute atom and the Fe atom that it replaced. For reference, the DDEC6 bond orders between Fe-atoms in the bulk were rated at 0.37 in the first coordination shell, and 0.15 in the second coordination shell.

When this summed bond order analysis is combined with the ANSBO cohesion analysis, η_{ANSBO}, it is possible to gain further insight into the nature of changed bonding induced by a solute and how it affects cohesion. An example demonstrating the usefulness of this combined analysis is if the cohesion at the weakest cleavage plane is weakened by a certain solute, but a relative increase in the total summed bond-orders compared to Fe is observed. Then, it may be inferred that the strengthening occurs in bonds in-plane and not cross-plane bonding, or that the bond-strengthening due to the segregated solute occurs in a different cleavage plane, or some combination of both.

2.5. Kinetics simulations

In order to assess the effects of thermomechanical processing on the segregation coverage of each of these solutes, we performed thermo-kinetic simulations. The kinetic segregation model couples the ab initio calculated segregation energies with the kinetics of a system. The model contains the segregation isotherm extended to multiple GB sites and multiple elements [70], the diffusivity of the segregating elements, and a minimal microstructure description of the system (namely the average grain size). This allows to assess the kinetics of segregation together with grain size effects and is much more representative of a real system than the typically used McLean isotherms. In this formulation, however, it is important to note that solute–solute interactions, beyond direct site-competition effects, are neglected. The methodology behind these kinetic simulations is described in full detail elsewhere [78].

The chosen conditions in the following emulate an isothermal-holding type heat treatment that is known to induce temper embrittlement in steels [1,4,79]. The exact simulated treatment was: austenisation at 1300 K, quenched at 50 K/s to 540 K, re-raised at 50 K/hr to 573/673/773/873 K, and then held isothermally for 28,000 h, and quenched to room temperature at 50 K/s. Note that solute–solute interactions at the GB were not accounted for in these simulations. The implications of this omission are presented and discussed in the latter Results and Discussions sections.

Regarding the alloying compositions considered, we assessed the Fe–P binary alloy, and the set of Fe–P-TM alloys, where TM is the set studied by our DFT calculations. The overall concentration of P was 0.01 at.% in all simulations. For the TM solutes, we assessed two different concentrations, 0.1 and 2.5 at.%. Consequently, the set of ternary alloys studied had compositions of Fe–TM-P (bal./ (0.1/2.5 at.%) / 0.01 at.%). For comparison, we also simulated the binary Fe–P (0.01 at.%) alloys. According to Bhadeshia's review of P-related embrittlement in steels [6], these are levels of phosphorus impurity and transition metal alloying concentrations that are commonly observed in industrial steels. The mean grain size in the simulations was 100 μm. We expect no significant effects due to grain-sizing on segregation coverage down to 5 μm. The diffusivities were taken from Versteylen et al. [80], who computed a consistent set of ab-initio diffusion data for TMs as well as P.

3. Results

3.1. Characteristic grain boundary quantities

The details regarding the four model GBs (number of atoms, n_{GB}, cell sizing with and without a vacuum) and certain GB quantities such as excess volume (V_{exc}), GB energy (γ_{GB}), smallest/largest calculated site Voronoi volumes ($V_{smallest}^{Vor}$, $V_{largest}^{Vor}$) are presented in Table 1. The quantities of excess volume and grain boundary energy of each of the four GBs are in very good agreement with the results calculated in Bhattacharya's prior study [62]. Note that there is a good correlation between the amount of excess volume at an interface and its GB energy, as has been observed frequently before [42,81].

3.2. Elemental segregation and cohesion effects

3.2.1. Segregation energies

To study the single-atom elemental segregation and its effects on the cohesion of the four model GBs, we profiled all the substitutional sites present at and near the interface [Fig. 2]. In the study of single-atom segregation to the $\Sigma11(3\bar{3}2)$ GB, we used a larger cell that had dimensions of 8.010 Å × 9.392 Å (2×2 compared to the cell presented in Table 1), due to interfacial reconstruction phenomena in the segregation profile. In the $\Sigma9(2\bar{2}1)$ GB, in generating the segregation profile of "P" we used a GB with transverse dimensions 8.010 Å × 6.332 Å (2×1 compared to the cell presented in Table 1) due to a reconstruction effect

Table 1

The sizes of the cells used in this study, the number of atoms in the bulk slab and GB cells, and their corresponding GB quantities of excess volume v_{exc} and GB energy (γ_{GB}) are presented. Excess volume and GB energy calculations were conducted using GB cells without vacuum, i.e. as presented in Fig. 1. The smallest and largest sites by Voronoi volume, $V^{Vor}_{smallest}$ and $V^{Vor}_{largest}$, within 3 Å of the interface plane are presented. All other calculations in the study were conducted using the GB+vacuum cells.

System	n_{GB}	m_{SLAB}	a (Å)	b (Å)	c_{GB} (Å)	c_{GB+vac} (Å)	V_{exc} (Å)	$V^{Vor}_{smallest}$ (Å^3)	$V^{Vor}_{largest}$ (Å^3)	γ_{GB} (J/m^2)	W_{sep} (J/m^2)
$\Sigma 3[110](1\bar{1}1)$	72	72	4.005	6.937	30.032	44.144	0.301	11.22	13.15	1.58	3.81
$\Sigma 3[110](1\bar{1}2)$	48	48	4.005	4.905	27.995	41.620	0.124	11.45	11.83	0.45	4.72
$\Sigma 9[110](2\bar{2}1)$	68	70	4.005	6.332	33.595	50.973	0.279	10.66	13.86	1.75	3.60
$\Sigma 11[110](3\bar{3}2)$	42	44	4.005	4.696	25.838	50.973	0.240	11.24	13.05	1.45	3.83

in the smaller cell. Further discussion may be found in the S.I. regarding this particular interface reconstruction effect. Segregation of solutes to the tightly-packed $\Sigma 3(1\bar{1}2)$ twin GB is generally unlikely due to the small magnitude of E_{seg} values. In the other GBs, which represent more generic types of GBs with more open structures, the segregation binding of P is significantly stronger than any of the TMs. The segregation likelihood is as follows, among P and the ten TMs: P $\gg$ Nb > Ti, Mn, Cu > Ni > Mo, W > V, Cr, Co. V, Cr and Co exhibit very small segregation binding tendencies, and are therefore generally significantly less likely to be found segregated at GBs compared to the other solutes at GBs.

From the segregation profiles plotted [Fig. 2], it is evident that certain types of solutes prefer different kinds of sites. For example, large solutes such as Mo, W prefer the site at the GB plane in the $\Sigma 3(1\bar{1}1)$ GB, whereas P prefers the site next to the GB plane. The reason for this is the smaller Voronoi volume of the site, which is preferable for solutes smaller than the Fe host atoms (e.g. P), and undesirable for larger atoms (Mo, W). We refer readers interested in this phenomenon to the supplementary information of our previous work [42].

It is mostly assumed in the literature that P occupies interstitial sites at GBs, but from our calculated values of segregation energies for P ($E_{seg} < -1$ eV for all but the $\Sigma 3(1\bar{1}2)$), it is clear that strong segregation binding exists for P at substitutional sites at GBs. We have extensively considered the available interstitial sites for P for all GBs in this study [see Supplementary Fig. S2]. However, we find that interstitial segregation is generally not favoured in all GBs except for the $\Sigma 3(1\bar{1}1)$ GB, where there is one site situated in the polyhedral void at the interface, with $E_{seg} = -1.05$ eV. This site is still less favourable than the substitutional site at the interface, which has $E_{seg} = -1.15$ eV. The segregation energy for the same interstitial site in the $\Sigma 3(1\bar{1}1)$ is $E_{seg} = -0.85$ eV in Yamaguchi et al.'s study [34]. The discrepancy in energy may be attributed to the larger cross-sectional area in their cell, which is two times larger in the "a" direction. As such, our simulated coverage of P is two times higher at one atom present in our cell, which results in a volume shrinkage effect that results in the lower calculated value of segregation energy in our cell. In the case of the $\Sigma 9(2\bar{2}1)$ and $\Sigma 11(3\bar{3}2)$ GBs, which possess merged sites, we find that when P is placed interstitially, the interface structure tends to relax into a configuration that is equivalent to GBs with substitutionally segregated P. This suggests that P prefers the substitutional position when segregated at these GBs. In the close-packed structure of the $\Sigma 3(1\bar{1}2)$ GB, we find that no interstitial sites are favourable, due to positive calculated values of E_{seg} in all considered configurations. These results indicate that the substitutional position is preferred in all GBs studied here. Importantly, we note that Yamaguchi et al. have found that the interstitial position is unfavourable in high concentration scenarios of P for the $\Sigma 3(1\bar{1}1)$ GB, through an incremental energetics study that revealed repulsion between P atoms. Due to these factors, we do not consider the interstitial P case in the following co-segregation study.

Larger transverse cell sizes (resulting in lower P concentration at the GB) in the model GBs may result in a different final relaxed atomic structure for interstitial P, but are not studied here due to the computational cost limitations. However, our study of the segregation behaviour of P in larger $\Sigma 9(2\bar{2}1)$ and $\Sigma 11(3\bar{3}2)$ cells shows that interface reconstructions after atomic relaxation may still occur, in spite of the large distance between solute atoms in larger cells [see Supplementary Fig. S10]. As such, we do not believe that the relaxation of P from

interstitial site into substitutional sites in the $\Sigma 9(2\bar{2}1)$ and $\Sigma 11(3\bar{3}2)$ is necessarily a result of the higher in-layer concentration due to smaller cells, but a real physical effect that results in P being relaxed into a substitutional site.

3.2.2. Cohesion in the Rice–Thomson–Wang framework

The cohesion effects as calculated in the Rice–Thomson–Wang framework are plotted against their segregation tendency in Fig. 3. The segregation tendency was quantified as the minimum E_{seg} (most negative value) across all profiled sites. To ensure segregation sites with very similar energies were not excluded from the cohesion analysis, we also calculated the effects where solutes are situated at sites within 0.05 eV of the minimum E_{seg} value. We considered the cohesion in both the rigid (η_{RGS}) and relaxed (η_{rel}) separation frameworks, as presented in Figs. 3(a), 4(a) and 3(b), 4(b) respectively. The full datasets are presented in the Supplementary Information (S.I.) in Tables S11–S14. In Fig. 3, we plot the segregation tendency for each solute against their effect on cohesion (η). We plot an absolute measure of cohesion for the GBs with each solute segregated, the work of separation (W_{sep}), against their segregation tendency in Fig. 4.

The calculated results in the Rice–Thomson–Wang framework indicate that segregated P is significantly detrimental to cohesion in the twin-like $\Sigma 3(1\bar{1}2)$ GB, moderately detrimental in the case of the $\Sigma 3(1\bar{1}1)$ and $\Sigma 9(2\bar{2}1)$ GBs, and neutral in the $\Sigma 9(1\bar{1}2)$. The calculated cohesion effect is -0.21 J/m^2 at 3.6 atoms/nm^2 for P in the $\Sigma 3(1\bar{1}1)$ GB, which is in good agreement with the -0.15 J/m^2 at 3.6 atoms/nm^2 coverage calculated in Yamaguchi's study for the same GB [82]. The TM results have been previously compared against the literature in our previous work [42]. Note that where P acts detrimentally on GB cohesion, its effect is similar quantitatively to the effect calculated for Cu. The significantly detrimental effect in the $\Sigma 3(1\bar{1}2)$ GB is paired with a low segregation tendency. The induced cohesion behaviour for the segregated TMs here has been presented previously [42]. To summarise, V, Cr, Co are generally neutral for GB cohesion. Mo and W are strong cohesion enhancers across all GBs. Ni exhibits a mixed effect on cohesion, and Cu is an embrittler. Mn, Nb and Ti exhibit various cohesion effects, ranging from neutral to significant cohesion enhancement, dependent on the local interface structure at the GB.

3.2.3. Cohesion in the bond-order framework

We used the DDEC6 bond-order framework to assess the strength of interface cohesion, through computing the ANSBO present at all the tested cleavage planes in the Rice–Thomson–Wang calculations. The results calculated in the bond-order framework of ANSBO and η_{ANSBO} are presented in Fig. 5.

The results attained from our bonding analysis in Fig. 5 are compared with the Rice–Thomson–Wang predictions [Figs. 3, 4]. The well-known GB cohesion enhancers of Mo and W significantly strengthen the immediate bonding in the local vicinity when segregated, which is responsible for the increase in η_{ANSBO}. This is the fundamental atomistic mechanism behind the increased resistance to intergranular fracture that these elements induce in steels. These results for Mo and W are consistent with those calculated in the Rice–Thomson–Wang framework. The elements of Co, Cr and V are mostly neutral for GB cohesion, which is also in agreement with the calculated Rice–Thomson–Wang results. Cu is found to be purely embrittling, which is also in agreement.
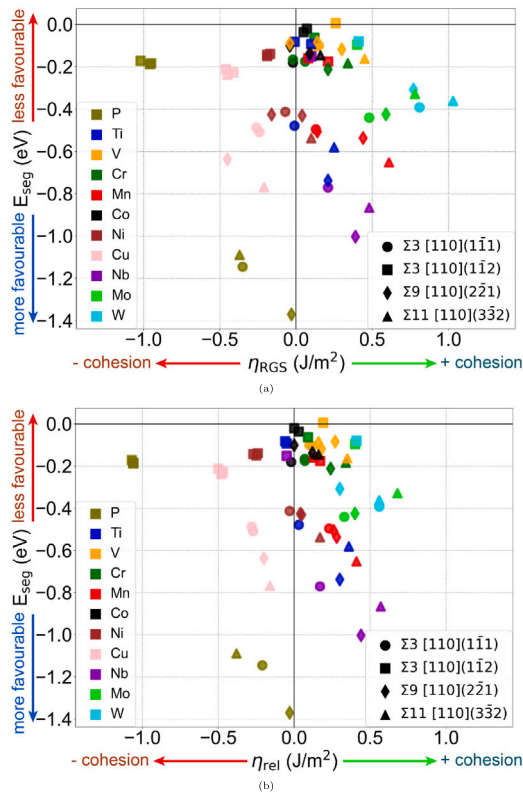
Fig. 3. The effects of single segregated solutes on GB cohesion, quantified by the changes in the works of separation (η) in the Rice–Thomson–Wang theory, are plotted against their tendency to segregate to each GB, represented by the segregation energy at the most favourable site (E_{seg}^{min}). 3(a) The cohesion effects calculated in the *rigid* separation framework. 3(b) The cohesion effects calculated in the *relaxed* separation framework. The data is tabulated in Supplementary Tables S11–S14.

Fig. 4. The absolute cohesion of GBs, in the pure and single solute segregation cases, quantified by the works of separation (W_{sep}), are plotted against the single-atom elemental tendencies to segregate to each GB, represented by the segregation energy at the most favourable site for binding (E_{seg}^{min}). 4(a) The W_{sep}^{RGS} calculated in the *rigid* separation framework. 4(b) The W_{sep} calculated in the *relaxed* separation framework. The data is tabulated in Supplementary Tables S11–S14.

However, beyond these results, there are also notable differences in the predicted cohesion effects in either framework. Mn has a mixed effect on cohesion from a bonding perspective, as opposed to being purely beneficial to cohesion in the Rice–Thomson–Wang framework. Ni is found to be mostly embrittling, compared to the mixed effect predicted in the Rice–Thomson–Wang framework. Ti is predicted to be mostly neutral/embrittling, compared to neutral/cohesion enhancing in the Rice–Thomson–Wang framework. Pure elemental segregation of P is predicted to have a neutral-to-moderate cohesion enhancing effect across the varying GBs studied here. This contradicts the neutral-embrittling effect found in the Rice–Thomson–Wang theory for P. We speculate that the particularly large difference in effects for P in the two frameworks can partially be attributed to the large surface relaxations that occur due to its significantly smaller size compared to the TMs and Fe. This in turn affects the computed RTW results due to the surface energy component. However, it is unclear as to whether this should be physically relevant to fracture at all [56]. A detailed assessment of why the differences exist in the two cohesion evaluation frameworks is presented in the Discussion.

Note that the changes in the bond-orders induced locally by a segregated solute do not necessarily induce corresponding changes in the cohesion of the GB [Fig. 5(c)]. While effects on interface cohesion such as those enacted by segregated Cu, Ni, Mo and W, can easily be attributed to immediately weakened/strengthened bonding due to the solute, the effects for some other solutes are not as obvious. For example, Nb increases the summed bond order of the atoms bonded to the segregated atom, but this may not necessarily increase the ANSBO across the weakest plane. This may be easily rationalised: bonds that were strengthened may not necessarily pass through the cleavage plane,
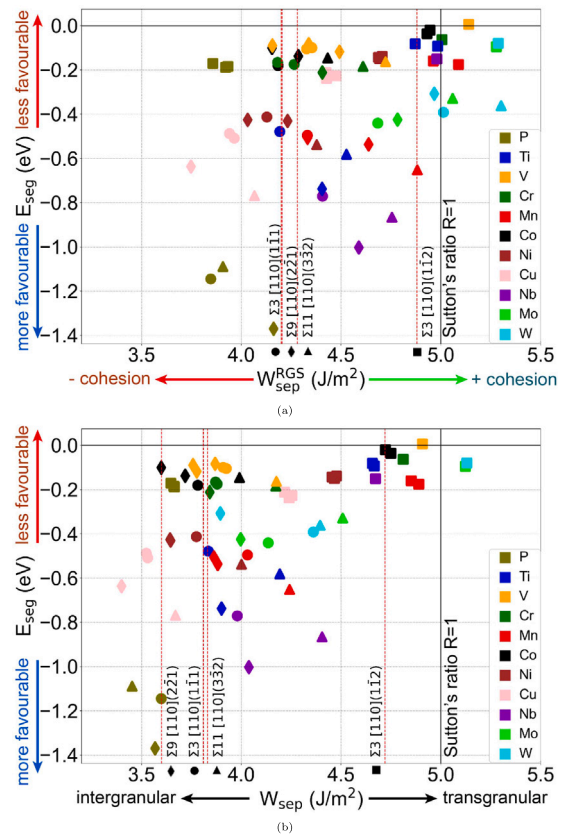
and instead could be those parallel to the GB plane, or increase the strength of bonds not in the weakest cleavage plane, and therefore not play a role in intergranular cleavage resistance. The remaining solutes of Ti, V, Cr, Mn and Co all induce relatively small changes in the summed bond order compared to the Fe atoms that they replace, although their effects on cohesion may vary.

The calculated cohesion effects in the bond-order based framework are highly sensitive to the positioning of segregated solutes, which is contrasted with the W_{sep} results, which were position-agnostic. Examples include that of the η_{ANSBO} of Ni in the $\Sigma 9(2\bar{2}1)$, Ti in the $\Sigma 3(11\bar{2})$, and Mn in the $\Sigma 9(2\bar{2}1)$. This is an intuitive result since the bonding states at the GB must change as a function of the *position* of segregated solutes. As a result, one would expect this changed bonding to correspondingly affect the cohesion at the interface. This effect is also present in a comparison of the η_{RGS} and η_{rel} quantities, in which the incorporation of surface relaxation can somewhat homogenise the calculated cohesion effects for the same solute, even when segregated in different positions at the GB. This fact can explain why η_{RGS} values are in generally better agreement with the η_{ANSBO} results. This also may be rationalised in a phenomenological sense, by understanding that the energy required to break bonds is better reflected by using the total energy of a non-equilibrium surface that is formed immediately after fracture (i.e. the rigid/unrelaxed surface) and the GB, rather than the final total energy of the equilibrium relaxed surface that is formed.

3.3. Co-segregation energetics and cohesion

The results of our co-segregation study are detailed in the following. In total, there were 44 P-X pairings considered in this study, with 10
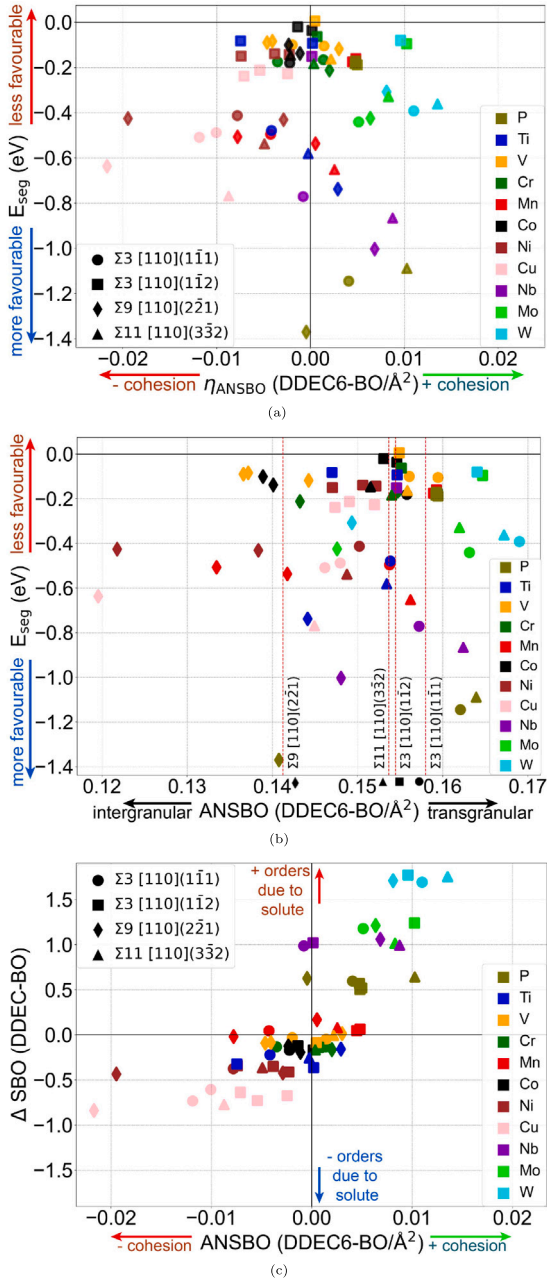
Fig. 5. The cohesion of GBs, in the pure and single solute segregation cases, as quantified by bond-orders, are plotted against the single-atom elemental tendencies to segregate to each GB (E_{seg}^{min}). 5(a) The cohesion effects, measured by differences in the calculated area-normalised summed bond orders at the pure and segregated GBs. 5(b) The absolute area-normalised summed bond orders across the weakest cleavage plane, as measured by bond-orders. 5(c) The area-normalised summed bond orders are plotted against the change in bond orders induced by the presence of the solute atom compared to the Fe atom in a pure GB. The data is tabulated in Supplementary Tables S11–S14.

TM-P pairs and the P–P co-segregation case, studied across the four GBs. Since the segregation sequence is also of significance, this results in a total of 84 co-segregation configurations that were considered in this study. We only considered the scenario where both P and X segregate to substitutional sites. The increased configurational complexity of studying co-segregation cases involving interstitial P-X requires larger cells and different GBs where interstitial P segregation is preferred over the substitutional sites [e.g. [37]]. This renders the computational cost
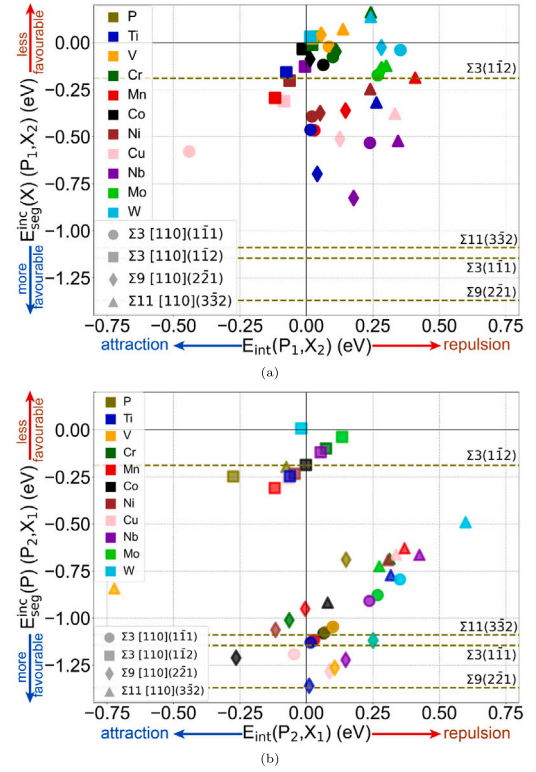

Fig. 6. The co-segregation likelihood of the second atom (E_{seg}^{inc}) in the P-X combinations is plotted against the interaction energies (E_{int}), for the most energetically likely configuration tested in each case. The incremental segregation likelihood of all elements is plotted against the P-X solute–solute interaction. This shows whether the co-segregation of the secondary segregating atom is encouraged ($E_{int} < 0$) or discouraged ($E_{int} > 0$) by the prior segregated atom, as well as the overall segregation likelihood of the second atom. In 6(a), the E_{seg}^{inc} is plotted for a secondary X atom segregating to a GB with P already segregated, and in 6(b), the E_{seg}^{inc} is plotted for P as a secondary segregating atom with X atom already present. The data is available in Supplementary Tables S15 and S16.

of including them in this study prohibitive at present, and hence we leave this for future work.

3.3.1. Co-segregation energetics

The *incremental* segregation energies (E_{seg}^{inc}) in all of the P-X and X-P co-segregation scenarios were computed. The *minimum* E_{seg}^{inc} calculated across all P-X and X-P configurations in each co-segregation scenario are plotted in Fig. 6, and tabulated in Supplementary Tables S15 and S16, respectively. The interactions that occur between solutes at the GB were quantified by calculation of the interaction energy (E_{int}). We plot the E_{int} data across all studied P-X and X-P co-segregation configurations in Fig. 7, as a function of solute–solute distance. The interaction energies at the minimum E_{seg}^{inc} configurations are tabulated in Supplementary Tables S15 and S16. This was done to determine how the interactions between solutes affect the favoured co-segregation scenario.

GBs with prior-segregated P are generally less favourable for co-segregation of any other solutes compared to a clean GB, due to repulsive P-X interactions [Fig. 6(a), Supplementary Table S16]. However, there are important exceptions. In cases such as the P–Cu in the $\Sigma 3(1\bar{1}1)$ GB or the P–P in the $\Sigma 3(1\bar{1}2)$, it can be seen that the presence of prior-segregated P actually has an extraordinary *attractive* interaction that causes strong co-segregation binding to occur, despite very weak segregation binding/non-binding at the same site in the pure GB. In these cases, the prior presence of P at the GB allows for a volume-shrinkage effect to occur at nearby sites at the GB surrounding the segregated P atom, which in turn, causes the neighbouring site at the
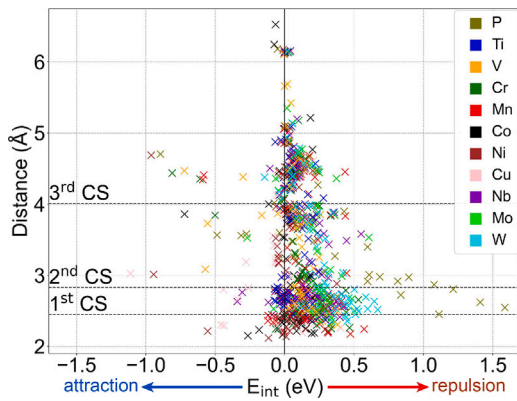
Fig. 7. The interaction energies (E_{int}) that occur between solutes at GBs are plotted as a function of solute–solute distance across all co-segregation positions considered. Per-GB and per-element plots are available in Supplementary Figs. S12–S13, respectively.

GB to become even more favourable for further P-cosegregation. Let us also note the large range of behaviours observed in some solute–solute interactions, with the same P–Cu sequenced pairing exhibiting $E_{int} = -0.44, -0.08, 0.13, 0.33$ eV in the minimum energy configurations for the $\Sigma3(1\bar{1}1)$, $\Sigma3(1\bar{1}2)$, $\Sigma9(2\bar{2}1)$ and $\Sigma11(3\bar{3}2)$ GBs, respectively. Note, however, $E_{int} = -0.05$ eV in the Cu-P sequenced pairing in the $\Sigma3(1\bar{1}1)$, showing that the order of co-segregation can also matter when considering these interactions. In the bulk, the P–Cu interactions are exclusively attractive in character, -0.15 eV $\leq E_{int} \leq 0.01$ eV [43].

The co-segregation of P is generally *discouraged* to GBs which are prior-decorated with segregated TM elements compared to pure GBs [Fig. 6(b), Supplementary Table S15]. However, despite these repulsive TM-P interactions, the absolute segregation likelihood, as quantified by E_{seg}^{inc}, nevertheless indicates that P still binds strongly to the GBs, with $E_{seg}^{inc} \leq -0.60$ eV in many cases. There is an exception to the repulsive P-TM interactions in the twin-like $\Sigma3(1\bar{1}2)$ GB, where the segregation of P in many cases is *slightly* encouraged, as indicated by our negative calculated E_{int} values. However, the absolute segregation likelihood of P to the $\Sigma3(1\bar{1}2)$ remains low in all considered co-segregation scenarios.

In Fig. 7, the entire calculated dataset of the E_{int} is plotted as a function of solute–solute distance. As can be seen, the interactions occurring between the studied TMs and P are mostly *repulsive* in nature ($E_{int} > 0$). We also plot the P-X interactions occurring in each GB in Supplementary Fig. S12, revealing that the local atomic structure can alter the nature and magnitude of the interactions significantly. In certain GBs, the same P-X pair interactions can range from significantly attractive to significantly repulsive in nature (e.g. the $\Sigma3(1\bar{1}1)$), but in others (e.g. the $\Sigma9(2\bar{2}1)$), they are almost exclusively repulsive. In Supplementary Fig. S13, we have additionally plotted the P-X interactions for each element individually and compared them to the interactions that occur in the bulk. It is evident that the P-X interactions calculated for the bulk are not an acceptable replacement for modelling the interactions at the GB. This is similar to the results found for TM–TM interactions previously [42]. The P-X interactions at GBs are intimately dependent on the local atomic structure and character of the GB in which they occur, diverging significantly from the interaction behaviours observed in the bulk.

3.3.2. The effect of co-segregation on cohesion

As in the single-solute segregation study, we similarly computed the effects of the co-segregated P-X and X-P pairs on GB cohesion, in both the Rice–Thomson–Wang framework and bonding-based DDEC6 assessment, respectively. The total segregation energy (E_{seg}^{tot}) of the co-segregated pair are plotted against their effects on GB cohesion (η) in Fig. 8. The Rice–Thomson–Wang data are plotted in the *rigid* and *relaxed* surface calculation frameworks in Figs. 8(a) and 8(b),
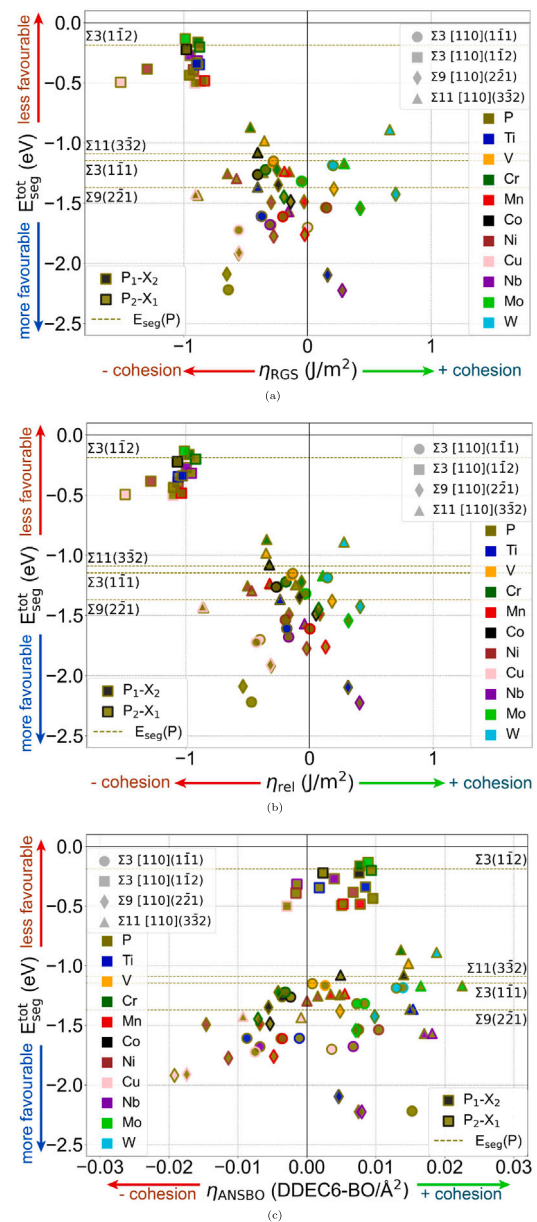

Fig. 8. The cohesion effects (η), calculated in various frameworks are plotted against the total energy of segregation of the co-segregated pair (E_{seg}^{tot}). The cohesion effects presented are calculated in the 8(a) Rice–Thomson–Wang rigid separation framework, 8(b) Rice–Thomson–Wang relaxed separation framework and 8(c) area-normalised summed DDEC6 bond-order framework. The data is available in Supplementary Tables S18–S21.

respectively. In Fig. 8(c) we plot the cohesion effects as quantified by the difference in the area-normalised bond-orders calculated in the DDEC6 bond-order framework.

In effect, the plots in Fig. 8 demonstrate the likelihood of co-segregation of a pair of elements to a particular type of GB, and their resultant induced effect on interface cohesion strength when co-segregated together at the GB. In general, more energetically favourable pairings, which are hence more likely to be found co-segregated, tend to be relatively worse for cohesion. This demonstrates a bias in the co-segregation phenomena towards pairings which are unfavourable for interface cohesion strength.

3.4. On synergistically complex cohesion effects in co-segregated P-X couples

Using our data, we may consider whether co-segregation of certain P-X combinations at a GB can enact effects on cohesion which are greater than the sum of their parts. This is achieved by comparing the actual computed effect of a co-segregated couple ($\eta_{P,X}$) to the summed effect of each individual component (i.e. linear superposition) ($\eta_P + \eta_X$). This can resolve whether certain P-TM couples (especially X = Mn/Cr/Ni) co-segregated couples can combine to enable a detrimental effect on ferritic Fe GB cohesion, as has long been speculated [1,23]. Mathematically, this statement takes the form:

$$\eta(P + X) \overset{?}{=} \eta(P) + \eta(X) \tag{14}$$

We term the difference between the quantities the heuristic error (ϵ):

$$\epsilon = \eta(P + X) - (\eta(P) + \eta(X)) \tag{15}$$

So, where $\eta(P + X) > \eta(P) + \eta(X)$ (i.e. $\epsilon > 0$), the cohesion of the GB is higher than expected from each of the solutes acting individually on cohesion, and where $\eta(P + X) < \eta(P) + \eta(X)$ (i.e. $\epsilon < 0$) the cohesion is lower than expected. The results of this comparison are plotted for each GB in Figs. 9(a), 9(b) and 9(c) for η_{RGS}, η_{rel} and η_{ANSBO}, respectively. From these plots, it becomes clear that the linear sum of effects is an acceptable approximation for the Rice–Thomson–Wang cohesion quantity of η_{rel}, is a very poor approximation in the case of the rigid Rice–Thomson–Wang quantity of η_{RGS}, and the bonding-based cohesion quantity of η_{ANSBO}. The plots of the heuristic error also demonstrate that there are no broad generalisations that may be drawn on whether combinations of P-TM couples are always better or worse for cohesion when co-segregated. Whether a co-segregated P-TM couple will have a better or worse effect on cohesion than the linear superposition of their individual solute effects depends instead on the GB structure that they are present at. The absolute cohesion effect of the co-segregated pairs is plotted alongside the linear superposition of their effects for comparison in Supplementary Fig. S17.

These results may be understood from the perspective of methodological implementation. The relaxed Rice–Thomson–Wang utilises the difference between the energies of the cells containing a GB with the two segregated solutes and the two *relaxed* surfaces that are formed after fracture. In this case, the energy of the two surfaces are frequently near-equivalent to those formed in the 1-solute segregation cases, leading to it being a relatively good approximation for the actual effect. Most of the observed differences therefore come from the GB contribution to the η_{rel}. In the case of the rigid Rice–Thomson–Wang implementation, η_{RGS} utilises the immediately as-cleaved structural configurations of the surfaces that are formed, without relaxation. Therefore, the surfaces formed are governed by their structure in the segregated/co-segregated GB. As such, the surfaces formed will have significantly different energies depending on their configuration at the GB, resulting in less homogenisation compared to the relaxed implementation. This leads to worse agreement in the heuristic quantity compared to the relaxed case. In the case of the bonding-based η_{ANSBO}, the poor agreement of the heuristic approximation must be understood from the fact that the model utilises bonding states to compute the cohesive strength of the interface. The fact that co-segregated solutes may have significantly different atomic bonding states (due to the presence of the other solute) compared to the bonding states in their single-solute cases naturally leads to the significant discrepancies observed in the heuristic approximation.

3.5. Kinetics

A high-level summary of the results from our kinetics simulations are presented in Figs. 10 and 11. The calculated diffusivities for each of the solutes at the temperatures of 573/673/773/873 K are presented in the Supplementary Table S22 and plotted in Supplementary Fig. S18.
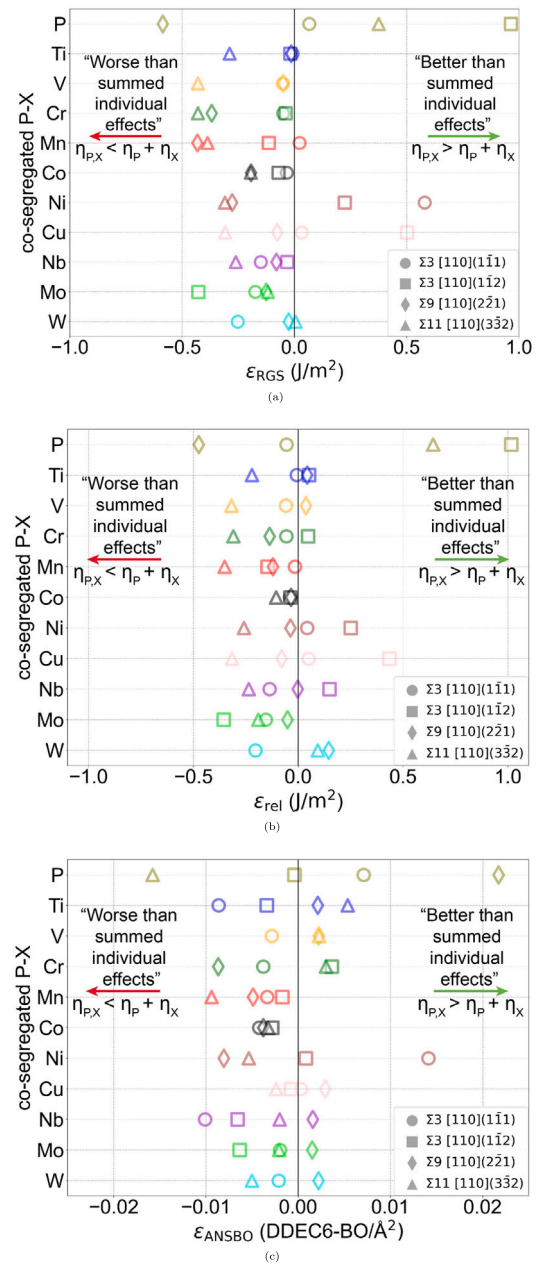

Fig. 9. The heuristic errors (ϵ), calculated in various frameworks are plotted for each co-segregating pair against the heuristic sum of each solute's individual effects on GB cohesion. These plots show the estimated effect from the linear sum of each solute's effects with respect to the actual calculated effect of the co-segregated pair. Only the cohesion effect calculated at the most energetically favourable pair-configuration (P-X vs X-P) is shown. No data is plotted in the cases where incremental segregation of the second solute is unfavourable in both pair configurations. This comparison is generated from the 9(a) Rice–Thomson–Wang rigid separation framework, 9(b) Rice–Thomson–Wang relaxed separation framework and 9(c) area-normalised summed DDEC6 bond-order framework. GB-specific plots with both configurations are presented in Supplementary Figs. S14–S16 in the S.I. The data is presented in Supplementary Tables S18–S21.

Here, it is important to emphasise that the models employed in this simulation did not account for the solute–solute interactions that occur between P and the transition metals. These interactions are generally mostly repulsive in the bulk and at the GB. There is one special case in the case of Cu–Cu, where strong attractive interactions in the bulk can cause clustering to occur in the bulk, and hence prevent segregation to the GBs [43]. This can significantly reduce the actual
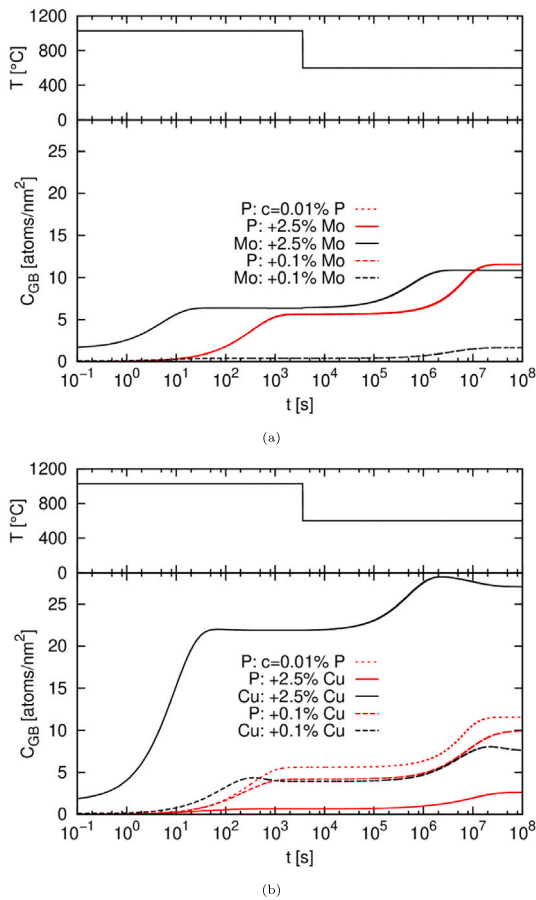
Fig. 10. The segregation coverage of solutes at the $\Sigma 11(3\bar{3}2)$ GB in Fe–P-TM ternary alloys are plotted against logarithmic time for the 600 °C isothermal holding variant of the simulated heat treatments in the kinetics framework. 10(a) The segregation coverage is plotted for the Fe–P–Mo ternary alloy variants. 10(b) The segregation coverage is plotted for the Fe–P–Cu ternary alloy variants. The presented concentrations are in atomic %. The full heat treatment is detailed in the main text.

observed coverage of Cu at the GBs. As such, one can assume that the coverage of TM solutes predicted by these simulations represents an upper bound for coverage. The real coverage is likely lower than predicted here by these simulations, which only accounts for direct site-competition effects. This is due to a combination of factors involving: phase-transformation fronts dragging P to ferritic GBs [83], that P-TM interactions being mostly repulsive [Figs. 6, 7], how P binds much more strongly to GBs than most TMs, and the fact that P is a much more mobile solute than any TM solute in α-Fe. Therefore the assumption that P generally occupies its favoured position at GBs should be fairly conservative. This is reflected in our time–temperature-coverage plot for the ternary Fe–Cu-P alloys in Fig. 10(b), where P eventually out-competes Cu at GBs, causing slight depletion of Cu at the GB at the end of the isothermal holding period.

In Fig. 10, the segregation coverage of solutes of Cu and Mo are plotted for the $\Sigma 11(3\bar{3}2)$ GB across the course of the simulated heat treatment with an isothermal holding temperature of 600 °C. One may observe that the segregation coverage for P in the Fe–P–Mo alloys is unaffected by the alloying concentration of Mo [Fig. 10(a)]. On the other hand, the segregation coverage of P is affected by the presence of Cu, and this is due to the preference of the same kind of alloying sites, leading to direct site competition between P and Cu. This is manifested in the lower segregation coverage of P as Cu content rises [Fig. 10(b)]. Importantly, note how the segregation coverage of P increases as a function of time, requiring significantly more time at isothermal holding periods to saturate compared to TMs, which observe a much faster and

smaller (in terms of increased coverage) saturation process. This is due to the lower bulk concentration of P, so for sufficient enrichment at the GB, atoms have to diffuse from farther away in the bulk.

In Fig. 11, the final segregation coverage of P and the TMs in each GB at the end of the heat treatments with the 300/400/500/600°C isothermal holding periods are plotted. There is no significant final segregation coverage of P at the $\Sigma 3(1\bar{1}2)$ GB at any heat treatment or ternary alloy composition; this is a result of the very weak segregation binding for all solutes at the GB. At $c_{TM} = 0.1$ at.%, there are no significant site-competition effects that occur between P and the TMs in all GBs. This may be attributed to the significantly stronger segregation binding that P exhibits to GBs, which manifests in almost no reduction in P segregation coverage at the GBs. At $c_{TM} = 2.5$ at.%, the segregation coverage of P may be moderately to significantly reduced in the set of Fe–P-(Cu/Ni/Mn) ternary alloys due to site-competition, dependent on GB type and heat treatment. Let us note that the site-competition effect manifests itself more strongly in the $\Sigma 9(2\bar{2}1)$ and $\Sigma 11(3\bar{3}2)$ GBs at high temperature regimes, but the reverse is true in the $\Sigma 3(1\bar{1}1)$ GB.

4. Discussion

To begin with, it is clear from the single-solute segregation profiles that P binds much more strongly to all GBs compared to the studied TMs, except for the special case of the twin-like $\Sigma 3(1\bar{1}2)$ GB. Therefore, the consistent presence of segregated P at intergranularly fractured surfaces, as often found previously with Auger electron spectroscopy [23], is almost certainly a result of its stronger segregation binding to GBs in comparison to the alloying metals. The consistent presence of P on these surfaces has caused many to deduce that it was the segregation of P alone that was responsible for the direct decohesion of the GBs, and hence temper embrittlement [1].

Our investigations into the elemental cohesive effects of P confirm that its segregation to ferritic Fe GBs, in isolation, is unlikely to be the underlying cause of P-induced temper embrittlement in steels. In the Rice–Thomson–Wang framework, the cohesive effect induced by segregated P is neutral-embrittling. However, GB character plays an important role in the effects of segregated P on cohesion in the Rice–Thomson–Wang framework. The effect of segregated P on W_{sep} is negligible in the $\Sigma 9(2\bar{2}1)$ GB, moderately detrimental in the $\Sigma 3(1\bar{1}1)$ and $\Sigma 11(3\bar{3}2)$ GBs, and significantly destructive to the cohesion of the $\Sigma 3(1\bar{1}2)$ GB. In a real alloy, the distribution of GBs is predominantly comprised of general GBs, as represented here by the $\Sigma 3(1\bar{1}1)$, $\Sigma 9(2\bar{2}1)$ and $\Sigma 11(3\bar{3}2)$ GBs, as opposed to special twin-like GBs, which are the archetype represented by the $\Sigma 3(1\bar{1}2)$. In the bond order framework, the effect of segregated P on cohesion is predicted to be neutral-cohesion enhancing. For reference, Cu is predicted to be a more powerful decohesion agent compared to P in all but one model general GB in both cohesion frameworks. These combined results indicate that direct P-induced embrittlement of GBs is unlikely to be the sole cause of induced temper embrittlement observed in ferritic steels. This finding is consistent with earlier works [1,4,23,34]. Recent experimental investigations have demonstrated that temper embrittlement can occur even at extremely low concentrations of P [46], or can be attributed to other factors [45], which supports these observations.

The kinetics-based simulations indicate that site-competition effects are only significant when solutes prefer the same kind of site at a GB. As such, the only solutes which exhibit significant competition with P are Cu, Mn and Ni. In the concentration regimes in which P is usually observed in steels (<0.01 at.%) the site competition effect is generally fairly small, when the concentration of Cu, Mn and Ni in the alloying composition is <0.1 at.%. The site competition effect becomes noticeable at concentrations of ~2.5 at.%, but only for Cu, Mn and Ni. So, in general, site competition effects are only significant when a combination of conditions is present. First, competing solutes must prefer the same kind of site at the GB. So, Nb, Mo, Ti, W, which prefer different kinds of substitutional sites compared to P, do not
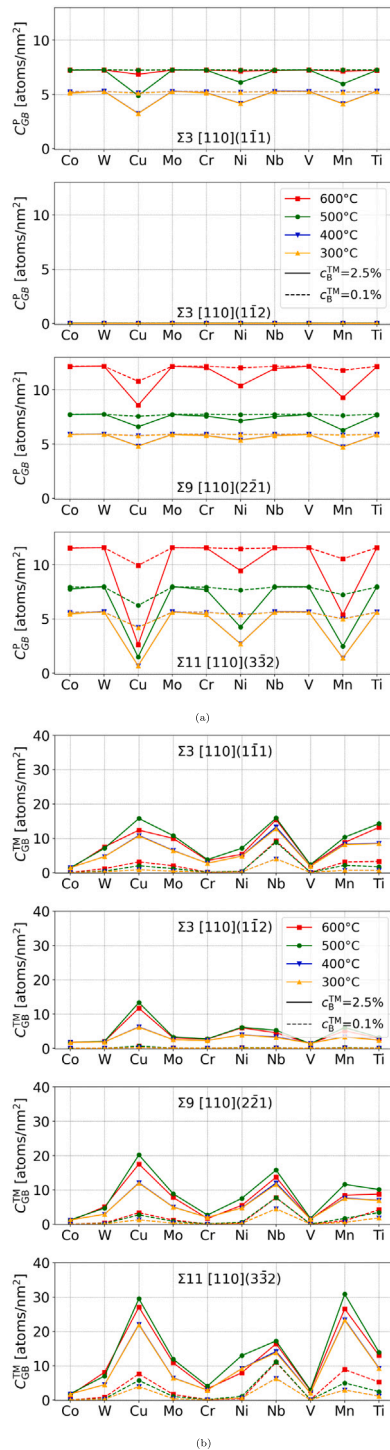
Fig. 11. The final interfacial segregation coverage of P and the TM solutes in each of the GBs at the end of each of the heat treatments simulated in this study. The heat treatments are distinguished by their different final isothermal holding temperatures of 300/400/500/600°C, for each of the ternary Fe–P-TM alloys considered. c_{GB} is the coverage of the solute at the GB, and c_B is the concentration of the solute in the bulk. The compositions considered for each of the ternary alloys are: c_B^P = 0.1 at.% P, c_B^{TM} = 0.1 at.%/2.5 at.% TM. 11(a) The final saturated segregation coverage of P (c_{GB}^P) in each of the Fe–P-TM alloys are plotted. 11(a) The final saturated segregation coverage of TM (c_{GB}^{TM}) in each of the Fe–P-TM alloys is plotted. Note that these are upper bounds for expected observed experimental coverage (see text). A comparison containing the TM coverage in the Fe–TM binary alloys undergoing the same heat treatments is presented in Supplementary Fig. S19.

compete with it, and hence do not reduce P-coverage directly through site competition, or vice-versa. Secondly, where the segregation binding of one solute is significantly weaker than the other, it must be present in a much higher concentration in the overall chemical composition to interfere with the segregation coverage of the stronger segregant. We can see this for Cu, Mn, and Ni, which although preferring the same site as P, when present at 0.1 at.%, do not impact segregation of P at 0.01 at.%, due to the significantly stronger P segregation binding. Observable effects on GB coverage of P are observed when c_{TM} = 2.5 at.%, but the relative attributable reduction due to site-competition is generally small, except in the case of the $\Sigma 11(3\bar{3}2)$ GB. So, in general, P, which has significantly stronger segregation tendencies than the TMs studied here, will not have its segregation coverage at GBs impeded significantly by site competition effects with common alloying solutes.

Although direct P-TM site-competition effects are not significant, this does not preclude the participation of other important co-segregation effects that may play a role in GB embrittlement. This can include the P-TM interactions that occur between solutes at GBs. In the model GBs that are closest in character to those that are often found in "real" alloys, i.e. general GBs ($\Sigma 3(1\bar{1}1)$, $\Sigma 9(2\bar{2}1)$ and $\Sigma 11(221)$), cohesion-enhancing solutes such as Mo and W experience significantly repulsive interactions with P. This reduces the co-segregation likelihood of Mo/W to almost negligible where P is already segregated. So, in GB regions that are rich with segregated P, we expect the segregation of Mo and W to be correspondingly reduced/depleted, not due to site competition, but via solute interactions. This should be taken alongside the fact that more energetically favourable P-TM couples are generally more detrimental to cohesion than the P–Mo/W couples. So acting in tandem, these factors can combine to enact a decohesive effect on cohesion.

Let us now consider the kinetics implications alongside the energetics mechanism proposed above. The P-TM co-segregation sequence is important, since it has been prior demonstrated experimentally that P-segregation is nigh-impossible (demonstrated at cooling rates up to 400 K/s) to suppress at ferritic GBs since P is accumulated and dragged at $\gamma \rightarrow \alpha$ phase transformation fronts [83]. This was attributed to the lower solubility of P in austenite. In this case, the repulsive nature of P-TM interactions significantly reduces the likelihood of a TM to segregate to GBs which were prior enriched with P, via the mentioned mechanism. The repulsive P–Mo/W interactions can then prevent the co-segregation of Mo/W to GBs, where P is already segregated. This allows for other, more energetically favourable P-TM pairs which are worse for interfacial cohesion to occupy the GB. This may be the mechanism by which P embrittles ferritic steels in the high P-concentration case, which would cause significant amounts of coverage to occur at GBs immediately after phase transformation. However, this mechanism is less likely to be operative in temper embrittlement phenomena, which are known to take prolonged exposure to higher temperature ranges to manifest [1].

In the case where P is the secondary segregating atom, its presence can eventually cause the depletion of prior-segregated cohesion enhancers. This scenario's importance is demonstrated by our kinetics simulations, which demonstrate that P enriches over time at GBs in the conditions known to facilitate temper embrittlement [Fig. 10]. Unlike the case where a TM solute is the secondary co-segregating atom, the repulsive P-TM interactions that occur at GBs are not enough to prevent significant co-segregation of P where TMs are already present. In this case, the fact that lower energy states can be attained in combination with non-Mo/W solutes is important. This allows other couples to occupy the GB (e.g. P–Cu, P-Ni, P–Mn), inducing relative embrittlement due to the depletion of cohesion-enhancing couples (e.g. P–Mo/P-W) from the GB. In the conditions which are known to induce temper embrittlement (slow cooling at/prolonged exposure to elevated temperatures), the enhanced solute mobility, slow enrichment of P at the interfaces (kinetics [Fig. 10]), and the subsequent relative depletion of cohesion enhancing couples from the GB can facilitate the commonly

observed embrittlement in ferritic GBs. This can cause the appearance of intergranular fracture modes in high strength steels, where GB cohesion can be the deciding factor in strength determination [6].

Whether co-segregated P-TM couples can enact or enable an embrittling effect on GB cohesion has long been the subject of speculation in the field [1,3,4,23]. In particular, the couples of P–Mn, P-Ni, and P-Cr were suspected to enact synergistically detrimental effects on GB cohesion when co-segregated [23]. However, our results across all cohesion calculation frameworks indicate that only the co-segregation of P with Mn is consistently worse for cohesion than their combined individual effects, regardless of the type of GB. If we only consider the results from the Rice–Thomson–Wang framework, P-Cr and P–Mo also exhibit such behaviour. However, both scenarios are generally unlikely to occur because of energetics considerations [Figs. 6, 8] and the prolonged exposure to heightened temperatures that are required to manifest embrittlement (i.e. higher solute mobility, resulting in the most energetically favourable equilibrium configurations to be attained at GBs). As such, P-Cr or P-Ni should not directly enact detrimental coupled effects on GB cohesion. P-Ni may cause the appearance of embrittlement simply by virtue of being more energetically favourable and being relatively worse for cohesion than other couples, in certain types of GBs. Co-segregated P-Cr couples are generally unlikely to occur at GBs, due to the very low segregation likelihood of Cr when accounting for the repulsive interactions with P. As such, Cr should not be an embrittler of GB cohesion, either as a standalone or acting in combination with P. Lastly, we note that co-segregated P–Cu couples are likely to be the most problematic for GB cohesion, due to a combination of high co-segregation likelihood and relatively worse cohesive effect, compared to other P-TM couples.

So, the combined factors of (a) an increase in P-coverage over time (kinetics), and (b) the strong repulsive P-TM interactions (energetics), can synergistically cause the commonly-observed temper embrittlement phenomena. In some specific cases, high initial coverage of P due to its strong segregation to GBs/phase transformation considerations (experiment [83]), and synergistically decohesive pairings (e.g. P–Mn) can also play a role. These factors combined can result in weakened interfacial cohesion due to P-enrichment at GBs in a ferritic steel. However, we note that certain P-TM combinations in the $\Sigma9(2\bar{2}1)$ GB can yield beneficial effects on cohesion, and are also energetically competitive with pairings which are relatively worse for cohesion (e.g. P–Ti, P–Nb). This yields an interesting opportunity for GB engineering, whereby manipulating the specific polyhedral atomic structure at GB interfaces to be similar to the $\Sigma9(2\bar{2}1)$ will allow segregation engineering of the interface. This may be achieved through the additions of Ti and Nb to a steel with such GB structures, which will create interfaces with segregation profiles which are specifically resistant to the deleterious mechanisms for cohesion associated with P-segregation, as proposed here.

Importantly, the results from our study allowed us to resolve some long-standing issues in the literature regarding temper embrittlement. First, we identify that attractive interactions causing favourable co-segregation of P-TMs are generally very rare, allowing us to disprove it as a proposed mechanism by which temper embrittlement operates [e.g. as proposed by Guttmann [19]]. Second, of the commonly studied P–(Ni/Mn/Cr) couples which are suspected to enact embrittlement when co-segregated together [e.g. as proposed by Briant [23]], only P–Mn is consistently worse for cohesion when segregated together. P–Ni/Cr couples are not always worse for cohesion acting together compared to individually, and instead, this depends on the specific GB structure to which they are co-segregated. Notably, co-segregated P–Cu is likely to be the most problematic for the embrittlement of ferritic Fe GBs. Lastly, from our kinetics results, we show that site-competition, at least between P and TMs, is unlikely to play a significant role in temper embrittlement phenomena.

It is important to acknowledge that idealised GB structural models are used in this study. Other effects, such as GB faceting, the formation of stepped and kinked structures in polycrystals may also play a role in the segregation phenomena studied here. However, previous studies have shown that segregation behaviours in symmetric tilt GBs can be representative for real general GBs (e.g. [84]). Furthermore, we study four different GBs with varying GB energies and structures, which represents an advancement to previously available work studying solute segregation in GBs. It is also notable that ⟨110⟩ GBs are more likely to occur in polycrystalline ferritic steels, and as such, the ⟨110⟩ models here should be representative to a certain degree for real GBs in steels [64]. Finally, we note that the study of the aforementioned effects in real GBs remains beyond the reach of DFT study at the time of this work mainly due to computational cost considerations. As such, their treatments are left for future work.

The differences in the predicted results for the effects of P and co-segregated P-X combinations on GB cohesion in the Rice–Thomson–Wang theory and the bond-order DDEC6 framework raise some important questions. The theory of Rice–Thomson–Wang [53,54] is the most widely employed model in the assessment of segregant effects on interface cohesion in the GB community. However, it assumes that fracture can be treated as an intrinsically thermodynamically reversible process. This assumption has been challenged on various grounds since its conception [56,57]. The cohesion effect of a solute is often computed as the difference between the segregation enthalpies of the solute to the surface and a GB. This is a comparison that has no physically intuitive link to fracture. If bond-orders, as computed in the DDEC6 framework [55], are an accurate tool for computing bond-strength, as is widely accepted in the quantum chemistry community [85], then the assessment of P to be embrittling from Rice–Thomson–Wang theory should be carefully re-examined. This has wide-reaching implications for all prior published literature studying interface cohesion that employed the Rice–Thomson–Wang theory of interfacial embrittlement. Intergranular fracture is controlled by the strength of bonds present at an interface — that much is indisputable. If the cohesion quantities calculated in the different frameworks are in conflict, then the quantity that has been demonstrated to be a powerful descriptor of bond-strength should be used, compared to a framework that contains thermodynamic assumptions that are intuitively inapplicable to fracture phenomena.

One may argue that the omission of consideration of co-segregation cases where P is located in interstitial positions leaves a gap in our assessment of its effects on GB cohesion. It may be conceded that elemental co-segregated P-TM couples with P situated in interstitial positions at GBs may yet induce the decohesive effects that were not seen in this study, which would be consistent with prior results [33]. However, let us note that our computed substitutional segregation energies for P of −1.03 eV→ −1.36 eV indicate that segregation binding at substitutional sites for P at GBs is extremely strong. P experiences significantly stronger segregation to substitutional sites at the studied GBs than TM solutes, which results in small observable site-competition effects, meaning that P is generally difficult to dislodge substitutionally purely through site-competition considerations at the GB [Fig. 11]. Note that the $\Sigma3(1\bar{1}1)$ GB has the largest excess volume of the GBs studied, and it is also the only GB which can host interstitially segregated P. It is the only GB where significantly attractive interactions between P-TM solutes occur. In the other three GBs, there is reduced excess volume available at the GB, which is generally indicative of reduced ability to host interstitially segregated solutes [74]. These combined factors mean that P atoms are much more likely to distribute themselves substitutionally over a larger GB area rather than concentrating locally and/or being pushed to occupy interstitial sites. Therefore, our results nevertheless represent a core advance in our understanding of complex P-TM co-segregation related phenomena and their role in the temper embrittlement of ferritic steels. Future work will focus on the co-segregation phenomena involving interstitial P and TMs, and their effects on the cohesion of ferritic Fe GBs.

5. Conclusions

We have performed an extensive DFT-based investigation of the segregation, co-segregation, kinetics, and cohesion behaviours of P and ten TMs. We first comprehensively evaluated the elemental segregation and cohesion behaviours of P and the ten TMs. We found that substitutional segregation was preferred by P in our model GBs, with only a single favourable interstitial site in the $\Sigma 3(1\bar{1}1)$ GB. We then scanned the configurational space in all co-segregation sequence scenarios, revealing that P-X solute–solute interactions are mostly repulsive in general/high-angle type GBs. It is also demonstrated that such interactions differ significantly from those observed in the bulk. The GB character and the local atomic structure play a critical role in determining the nature and magnitude of these interactions, which can range from slightly attractive to significantly repulsive. In general GBs, the P-X interactions are almost always repulsive. In the case of twin-like/stacking fault GBs, these interactions can be slightly attractive. The much faster diffusion of P relative to TMs and its strong segregation/co-segregation binding to GBs explains the experimental observations of its ubiquitous presence at intergranular fracture surfaces.

However, the role that P plays on cohesion cannot be reduced to a direct decohesion effect induced by weakened bonding when segregated. Instead, from our combined results, we propose that the P-embrittlement effect may instead be attributed to its strong segregation and co-segregation to GBs, and, critically, the repulsive P-X solute–solute interactions with strong cohesion enhancers (e.g. Mo, W). These repulsive interactions may cause a localised depletion of the cohesion-enhancing solutes at GBs, which may then allow more cohesion-detrimental pairings (e.g. P–Mn, P–Cu) to occupy the GB. When segregated in combination with Mn, the effect on cohesion is always more detrimental compared to their summed individual effects. These critical co-segregation effects may act in tandem to result in an overall relative reduction in the cohesion of GBs with enriched P, thereby contributing to the temper embrittlement of the steel. Finally, a contradiction for the predicted cohesion effects of segregated solutes in the Rice–Thomson–Wang theory of interfacial embrittlement compared to those derived from bond-orders in the DDEC6 framework was revealed and explained.

Declaration of competing interest

The authors declare that they have no known competing financial interests or personal relationships that could have appeared to influence the work reported in this paper.

Acknowledgements

Appendix A. Supplementary data

Supplementary material related to this article can be found online at https://doi.org/10.1016/j.actamat.2023.118850.

References

[1] V.V. Zabil'skii, Temper embrittlement of structural alloy steels (review), Met. Sci. Heat Treat. 29 (1) (1987) 32–42, http://dx.doi.org/10.1007/BF00735489.

[2] D. Kalderon, Steam turbine failure at Hinkley point 'A', Proc. Inst. Mech. Eng. 186 (1) (1972) 341–377, http://dx.doi.org/10.1243/PIME_PROC_1972_186_037_02.

[3] C.L. Briant, S.K. Banerji, Intergranularfailure in steel: The role of grain-boundary composition, Int. Met. Rev. 23 (1) (1978) 164–199, http://dx.doi.org/10.1179/imtr.1978.23.1.164.

[4] I. Olefjord, Temper embrittlement, Int. Met. Rev. 23 (1) (1978) 149–163, http://dx.doi.org/10.1179/imtr.1978.23.1.149.

[5] P. Lejček, M. Šob, V. Paidar, Interfacial segregation and grain boundary embrittlement: An overview and critical assessment of experimental data and calculated results, Prog. Mater. Sci. 87 (2017) 83–139, http://dx.doi.org/10.1016/j.pmatsci.2016.11.001.

[6] H.K.D.H. Bhadeshia, D.-W. Suh, Is low phosphorus content in steel a product requirement? Ironmak. Steelmak. 42 (4) (2015) 259–267, http://dx.doi.org/10.1179/1743281214Y.0000000261.

[7] J. LOW, D.F. Stein, A.M. Turkalo, R.P. Laforce, Alloy and impurity effects on temper brittleness of steel, Trans. Met. Soc. AIME 242 (1) (1968) 14–24.

[8] R.A. Mulford, C.J. Mcmahon, D.P. Pope, H.C. Feng, Temper embrittlement of Ni-Cr Steels by phosphorus, Metall. Trans. A 7 (8) (1976) 1183–1195, http://dx.doi.org/10.1007/BF02656602.

[9] B.C. Edwards, H.E. Bishop, J.C. Riviere, B.L. Eyre, An AES study of temper embrittlement in a low alloy steel, Acta Metall. 24 (10) (1976) 957–967, http://dx.doi.org/10.1016/0001-6160(76)90043-2.

[10] C.J. McMahon, Intergranular fracture in steels, Mater. Sci. Eng. 25 (1976) 233–239, http://dx.doi.org/10.1016/0025-5416(76)90075-6.

[11] E.D. Hondros, M.P. Seah, Segregation to interfaces, Int. Met. Rev. 22 (1) (1977) 262–301, http://dx.doi.org/10.1179/imtr.1977.22.1.262.

[12] J. Yu, C.J. McMahon, The effects of composition and carbide precipitation on temper embrittlement of 2.25 Cr-1 Mo steel: Part II. Effects of Mn and Si, Metall. Trans. A 11 (2) (1980) 291, http://dx.doi.org/10.1007/BF02660633.

[13] P. Lemblé, A. Pineau, J.L. Castagne, P. Dumoulin, Temper embrittlement in 12%Cr martensitic steel, Met Sci 13 (8) (1979) 496–502, http://dx.doi.org/10.1179/030634579790438381.

[14] J. Yu, C.J. McMahon, The effects of composition and carbide precipitation on temper embrittlement of 2.25 Cr-1 Mo steel: Part I. Effects of P and Sn, Metall. Trans. A 11 (2) (1980) 277–289, http://dx.doi.org/10.1007/BF02660632.

[15] M. Calcagnotto, D. Ponge, D. Raabe, On the effect of manganese on grain size stability and hardenability in ultrafine-grained ferrite/martensite dual-phase steels, Metall. Mater. Trans. A 43 (1) (2012) 37–46, http://dx.doi.org/10.1007/s11661-011-0828-3.

[16] Y. Yu, S. Shironita, K. Souma, M. Umeda, Effect of chromium content on the corrosion resistance of ferritic stainless steels in sulfuric acid solution, Heliyon 4 (11) (2018) e00958, http://dx.doi.org/10.1016/j.heliyon.2018.e00958.

[17] K.Y. Xie, T. Zheng, J.M. Cairney, H. Kaul, J.G. Williams, F.J. Barbaro, C.R. Killmore, S.P. Ringer, Strengthening from Nb-rich clusters in a Nb-microalloyed steel, Scr. Mater. 66 (9) (2012) 710–713, http://dx.doi.org/10.1016/j.scriptamat.2012.01.029.

[18] S.P. Ringer, W.B. Li, K.E. Easterling, On the interaction and pinning of grain boundaries by cubic shaped precipitate particles, Acta Metall. 37 (3) (1989) 831–841, http://dx.doi.org/10.1016/0001-6160(89)90010-2.

[19] M. Guttmann, Equilibrium segregation in a ternary solution: A model for temper embrittlement, Surf. Sci. 53 (1) (1975) 213–227, http://dx.doi.org/10.1016/0039-6028(75)90125-9.

[20] M. Guttmann, The link between equilibrium segregation and precipitation in ternary solutions exhibiting temper embrittlement, Met. Sci. 10 (10) (1976) 337–341, http://dx.doi.org/10.1179/030634576790431390.

[21] M. Guttman, The role of residuals and alloying elements in temper embrittlement, Philos. Trans. R. Soc. Lond. Ser. A Math. Phys. Sci. 295 (1413) (1997) 169–196, http://dx.doi.org/10.1098/rsta.1980.0099.

[22] M. Guttmann, P. Dumoulin, M. Wayman, The thermodynamics of interactive co-segregation of phosphorus and alloying elements in iron and temper-brittle steels, Metall. Trans. A 13 (10) (1982) 1693–1711, http://dx.doi.org/10.1007/BF02647825.

[23] C.L. Briant, The effect of nickel, chromium, and manganese on phosphorus segregation in low alloy steels, Scr. Metall. 15 (9) (1981) 1013–1018, http://dx.doi.org/10.1016/0036-9748(81)90245-3.

[24] H.J. Grabke, R. Möller, H. Erhart, S.S. Brenner, Effects of the alloying elements Ti, Nb, Mo and V on the grain boundary segregation of P in iron and steels, Surf. Interface Anal. 10 (4) (1987) 202–209, http://dx.doi.org/10.1002/sia.740100405.

[25] H.J. Grabke, K. Hennesen, R. Möller, W. Wei, Effects of manganese on the grain boundary segregation, bulk and grain boundary diffusivity of P in ferrite, Scr. Metall. 21 (10) (1987) 1329–1334, http://dx.doi.org/10.1016/0036-9748(87)90108-6.

[26] H.J. Grabke, Grain boundary segregation of impurities in iron and steels and effects on steel properties, in: Impurities in Engineering Materials, Routledge, 1999.

[27] R. Wu, A.J. Freeman, G.B. Olson, On the electronic basis of the phosphorus intergranular embrittlement of iron, J. Mater. Res. 7 (9) (1992) 2403–2411, http://dx.doi.org/10.1557/JMR.1992.2403.

[28] R. Wu, A.J. Freeman, G.B. Olson, First principles determination of the effects of phosphorus and boron on iron grain boundary cohesion, Science 265 (5170) (1994) 376–380, http://dx.doi.org/10.1126/science.265.5170.376.

[29] L.P. Sagert, G.B. Olson, D.E. Ellis, Chemical embrittlement of Fe grain boundaries: P and the P–Mo couple, Phil. Mag. B 77 (3) (1998) 871–889, http://dx.doi.org/10.1080/13642819808214840.

[30] Y.-Q. Fen, C.-Y. Wang, Electronic effects of nitrogen and phosphorus on iron grain boundary cohesion, Comput. Mater. Sci. 20 (1) (2001) 48–56, http://dx.doi.org/10.1016/S0927-0256(00)00124-5.

[31] R. Wu, A.J. Freeman, G.B. Olson, Nature of phosphorus embrittlement of the Fe Σ3[1-10](111) grain boundary, Phys. Rev. B 50 (1) (1994) 75–81, http://dx.doi.org/10.1103/PhysRevB.50.75.

[32] L. Zhong, R. Wu, A.J. Freeman, G.B. Olson, Effects of Mn additions on the P embrittlement of the Fe grain boundary, Phys. Rev. B 55 (17) (1997) 11133–11137, http://dx.doi.org/10.1103/PhysRevB.55.11133.

[33] W.T. Geng, A.J. Freeman, G.B. Olson, Influence of alloying additions on the impurity induced grain boundary embrittlement, Solid State Commun. 119 (10) (2001) 585–590, http://dx.doi.org/10.1016/S0038-1098(01)00298-8.

[34] M. Yamaguchi, Y. Nishiyama, H. Kaburaki, Decohesion of iron grain boundaries by sulfur or phosphorous segregation: First-principles calculations, Phys. Rev. B 76 (3) (2007) 035418, http://dx.doi.org/10.1103/PhysRevB.76.035418.

[35] E. Wachowicz, A. Kiejna, Effect of impurities on structural, cohesive and magnetic properties of grain boundaries in α-Fe 19(2), 2011, 025001, http://dx.doi.org/10.1088/0965-0393/19/2/025001.

[36] M. Yamaguchi, J. Kameda, Multiscale thermodynamic analysis on fracture toughness loss induced by solute segregation in steel, Phil. Mag. 94 (19) (2014) 2131–2149, http://dx.doi.org/10.1080/14786435.2014.906757.

[37] D. Scheiber, L. Romaner, Impact of the segregation energy spectrum on the enthalpy and entropy of segregation, Acta Mater. 221 (2021) 117393, http://dx.doi.org/10.1016/j.actamat.2021.117393.

[38] R.P. Messmer, C.L. Briant, The role of chemical bonding in grain boundary embrittlement, Acta Metall. 30 (2) (1982) 457–467, http://dx.doi.org/10.1016/0001-6160(82)90226-7.

[39] C.L. Briant, R.P. Messmer, An electronic model for the effect of alloying elements on the phosphorus induced grain boundary embrittlement of steel, Acta Metall. 30 (9) (1982) 1811–1818, http://dx.doi.org/10.1016/0001-6160(82)90097-9.

[40] T. Ogura, T. Watanabe, S. Karashima, T. Masumoto, Dependence of phosphorus segregation on grain boundary crystallography in an Fe–Ni–Cr alloy, Acta Metall. 35 (7) (1987) 1807–1814, http://dx.doi.org/10.1016/0001-6160(87)90126-X.

[41] W.-S. Ko, N.J. Kim, B.-J. Lee, Atomistic modeling of an impurity element and a metal–impurity system: Pure P and Fe–P system, J. Phys.: Condens. Matter 24 (22) (2012) 225002, http://dx.doi.org/10.1088/0953-8984/24/22/225002.

[42] H.L. Mai, X.-Y. Cui, D. Scheiber, L. Romaner, S.P. Ringer, The segregation of transition metals to iron grain boundaries and their effects on cohesion, Acta Mater. 231 (2022) 117902, http://dx.doi.org/10.1016/j.actamat.2022.117902.

[43] O. Gorbatov, A. Hosseinzadeh Delandar, Y. Gornostyrev, A. Ruban, P. Korzhavyi, First-principles study of interactions between substitutional solutes in bcc iron, J. Nucl. Mater. 475 (2016) 140–148, http://dx.doi.org/10.1016/j.jnucmat.2016.04.013.

[44] D. Scheiber, L. Romaner, R. Pippan, P. Puschnig, Impact of solute-solute interactions on grain boundary segregation and cohesion in molybdenum, Phys. Rev. Mater. 2 (9) (2018) 093609, http://dx.doi.org/10.1103/PhysRevMaterials.2.093609.

[45] F. Nikbakht, M. Nasim, C. Davies, E.A. Wilson, H. Adrian, Isothermal embrittlement of Fe–8Mn alloys at 450°C, Mater. Sci. Technol. 26 (5) (2010) 552–558, http://dx.doi.org/10.1179/174328409X405616.

[46] M. Kuzmina, D. Ponge, D. Raabe, Grain boundary segregation engineering and austenite reversion turn embrittlement into toughness: Example of a 9wt.% medium Mn steel, Acta Mater. 86 (2015) 182–192, http://dx.doi.org/10.1016/j.actamat.2014.12.021.

[47] D. Raabe, B. Sun, A. Kwiatkowski Da Silva, B. Gault, H.-W. Yen, K. Sedighiani, P. Thoudden Sukumar, I.R. Souza Filho, S. Katnagallu, E. Jägle, P. Kürnsteiner, N. Kusampudi, L. Stephenson, M. Herbig, C.H. Liebscher, H. Springer, S. Zaefferer, V. Shah, S.-L. Wong, C. Baron, M. Diehl, F. Roters, D. Ponge, Current challenges and opportunities in microstructure-related properties of advanced high-strength steels, Metall. Mater. Trans. A 51 (11) (2020) 5517–5586, http://dx.doi.org/10.1007/s11661-020-05947-2.

[48] K.H. Kwon, I.C. Yi, Y. Ha, K.K. Um, J.K. Choi, K. Hono, K. Oh-ishi, N.J. Kim, Origin of intergranular fracture in martensitic 8Mn steel at cryogenic temperatures, Scr. Mater. 69 (5) (2013) 420–423, http://dx.doi.org/10.1016/j.scriptamat.2013.05.042.

[49] M. Nasim, B.C. Edwards, E.A. Wilson, A study of grain boundary embrittlement in an Fe–8%Mn alloy, Mater. Sci. Eng. A 281 (1) (2000) 56–67, http://dx.doi.org/10.1016/S0921-5093(99)00734-0.

[50] K. Ito, H. Sawada, S. Ogata, First-principles study on the grain boundary embrittlement of bcc-Fe by Mn segregation, Phys. Rev. Mater. 3 (1) (2019) 013609, http://dx.doi.org/10.1103/PhysRevMaterials.3.013609.

[51] A.S. Kholtobina, W. Ecker, R. Pippan, V.I. Razumovskiy, Effect of alloying elements on hydrogen enhanced decohesion in bcc iron, Comput. Mater. Sci. 188 (2021) 110215, http://dx.doi.org/10.1016/j.commatsci.2020.110215.

[52] A. P. A. Subramanyam, A. Azócar Guzmán, S. Vincent, A. Hartmaier, R. Janisch, Ab initio study of the combined effects of alloying elements and H on grain boundary cohesion in ferritic steels, Metals 9 (3) (2019) 291, http://dx.doi.org/10.3390/met9030291.

[53] J.R. Rice, R. Thomson, Ductile versus brittle behaviour of crystals, Phil. Mag. J. Theor. Exp. Appl. Phys. 29 (1) (1974) 73–97, http://dx.doi.org/10.1080/14786437408213555.

[54] J.R. Rice, J.-S. Wang, Embrittlement of interfaces by solute segregation, Mater. Sci. Eng. A 107 (1989) 23–40, http://dx.doi.org/10.1016/0921-5093(89)90372-9.

[55] T.A. Manz, Introducing DDEC6 atomic population analysis: Part 3. Comprehensive method to compute bond orders, RSC Adv. 7 (72) (2017) 45552–45581.

[56] C.L. Briant, On the chemistry of grain boundary segregation and grain boundary fracture, Metall. Trans. A 21 (9) (1990) 2339–2354, http://dx.doi.org/10.1007/BF02646981.

[57] C.J. McMahon, V. Vitek, G.R. Belton, On the theory of embrittlement of steels by segregated impurities, Scr. Metall. 12 (9) (1978) 785–789, http://dx.doi.org/10.1016/0036-9748(78)90036-4.

[58] P.E. Blöchl, Projector augmented-wave method, Phys. Rev. B 50 (24) (1994) 17953–17979, http://dx.doi.org/10.1103/PhysRevB.50.17953.

[59] G. Kresse, J. Furthmüller, Efficiency of Ab-initio total energy calculations for metals and semiconductors using a plane-wave basis set, Comput. Mater. Sci. 6 (1) (1996) 15–50, http://dx.doi.org/10.1016/0927-0256(96)00008-0.

[60] G. Kresse, J. Furthmüller, Efficient iterative schemes for Ab initio total-energy calculations using a plane-wave basis set, Phys. Rev. B 54 (16) (1996) 11169–11186, http://dx.doi.org/10.1103/PhysRevB.54.11169.

[61] J.P. Perdew, K. Burke, M. Ernzerhof, Generalized gradient approximation made simple, Phys. Rev. Lett. 77 (18) (1996) 3865–3868, http://dx.doi.org/10.1103/PhysRevLett.77.3865.

[62] S.K. Bhattacharya, S. Tanaka, Y. Shiihara, M. Kohyama, Ab initio perspective of the ⟨110⟩ symmetrical tilt grain boundaries in bcc Fe: Application of local energy and local stress, J. Mater. Sci. 49 (11) (2014) 3980–3995, http://dx.doi.org/10.1007/s10853-014-8038-1.

[63] H. Nakashima, M. Takeuchi, Grain boundary energy and structure of α-Fe<110>symmetric tilt boundary, Tetsu-to-Hagané 86 (5) (2000) 357–362, http://dx.doi.org/10.2355/tetsutohagane1955.86.5_357.

[64] S.K. Bhattacharya, S. Tanaka, Y. Shiihara, M. Kohyama, Ab initio study of symmetrical tilt grain boundaries in bcc Fe: Structural units, magnetic moments, interfacial bonding, local energy and local stress, J. Phys.: Condens. Matter 25 (13) (2013) 135004, http://dx.doi.org/10.1088/0953-8984/25/13/135004.

[65] A.H. Larsen, J.J. Mortensen, J. Blomqvist, I.E. Castelli, R. Christensen, M. Dułak, J. Friis, M.N. Groves, B. Hammer, C. Hargus, E.D. Hermes, P.C. Jennings, P.B. Jensen, J. Kermode, J.R. Kitchin, E.L. Kolsbjerg, J. Kubal, K. Kaasbjerg, S. Lysgaard, J.B. Maronsson, T. Maxson, T. Olsen, L. Pastewka, A. Peterson, C. Rostgaard, J. Schiøtz, O. Schütt, M. Strange, K.S. Thygesen, T. Vegge, L. Vilhelmsen, M. Walter, Z. Zeng, K.W. Jacobsen, The atomic simulation environment—a Python library for working with atoms, J. Phys.: Condens. Matter 29 (27) (2017) 273002, http://dx.doi.org/10.1088/1361-648X/aa680e.

[66] D. Wolf, Structure-energy correlation for grain boundaries in f.c.c. metals—II. Boundaries on the (110) and (113) planes, Acta Metall. 37 (10) (1989) 2823–2833, http://dx.doi.org/10.1016/0001-6160(89)90317-9.

[67] D. Wolf, Structure-energy correlation for grain boundaries in f.c.c. metals—I. Boundaries on the (111) and (100) planes, Acta Metall. 37 (7) (1989) 1983–1993, http://dx.doi.org/10.1016/0001-6160(89)90082-5.

[68] V.I. Razumovskiy, A.Y. Lozovoi, I.M. Razumovskii, First-principles-aided design of a new Ni-base superalloy: Influence of transition metal alloying elements on grain boundary and bulk cohesion, Acta Mater. 82 (2015) 369–377, http://dx.doi.org/10.1016/j.actamat.2014.08.047.

[69] D. McLean, A. Maradudin, Grain boundaries in metals, Phys. Today 11 (1958) 35, http://dx.doi.org/10.1063/1.3062658.

[70] C.L. White, W.A. Coghlan, The spectrum of binding energies approach to grain boundary segregation, Metall. Trans. A 8 (9) (1977) 1403–1412, http://dx.doi.org/10.1007/BF02642853.

[71] H. Jin, I. Elfimov, M. Militzer, Study of the interaction of solutes with $\Sigma 5$ (013) tilt grain boundaries in iron using density-functional theory, J. Appl. Phys. 115 (9) (2014) 093506, http://dx.doi.org/10.1063/1.4867400.

[72] T. Nenninger, F. Sansoz, Local atomic environment analysis of short and long-range solute-solute interactions in a symmetric tilt grain boundary, Scr. Mater. 222 (2023) 115045, http://dx.doi.org/10.1016/j.scriptamat.2022.115045.

[73] A. Tehranchi, W.A. Curtin, Atomistic study of hydrogen embrittlement of grain boundaries in nickel: I. Fracture, J. Mech. Phys. Solids 101 (2017) 150–165, http://dx.doi.org/10.1016/j.jmps.2017.01.020.

[74] H.L. Mai, X.-Y. Cui, D. Scheiber, L. Romaner, S.P. Ringer, An understanding of hydrogen embrittlement in nickel grain boundaries from first principles, Mater. Des. 212 (2021) 110283, http://dx.doi.org/10.1016/j.matdes.2021.110283.

[75] M.E. Fernandez, R. Dingreville, D.E. Spearot, Statistical perspective on embrittling potency for intergranular fracture, Phys. Rev. Mater. 6 (8) (2022) 083602, http://dx.doi.org/10.1103/PhysRevMaterials.6.083602.

[76] A.P. Sutton, Interfaces in Crystalline Materials, in: Monographs on the Physice and Chemistry of Materials, Clarendon Press, 1995, pp. 414–423.

[77] A. Pineau, A.A. Benzerga, T. Pardoen, Failure of metals I: Brittle and ductile fracture, Acta Mater. 107 (2016) 424–483, http://dx.doi.org/10.1016/j.actamat.2015.12.034.

[78] D. Scheiber, L. Romaner, F.D. Fischer, J. Svoboda, Kinetics of grain boundary segregation in multicomponent systems – The example of a Mo-C-B-O system, Scr. Mater. 150 (2018) 110–114, http://dx.doi.org/10.1016/j.scriptamat.2018.03.011.

[79] R. Chaouadi, J. Van Eyken, R. Gérard, M. Lambrecht, I. Uytdenhouwen, Effect of step cooling and P-segregation to grain boundaries on the tensile and fracture toughness properties of A533B plate and A508 forging steels, J. Nucl. Mater. 550 (2021) 152924, http://dx.doi.org/10.1016/j.jnucmat.2021.152924.

[80] C.D. Versteylen, N.H. van Dijk, M.H.F. Sluiter, First-principles analysis of solute diffusion in dilute bcc Fe–X alloys, Phys. Rev. B 96 (9) (2017) 094105, http://dx.doi.org/10.1103/PhysRevB.96.094105.

[81] D.L. Olmsted, S.M. Foiles, E.A. Holm, Survey of computed grain boundary properties in face-centered cubic metals: I. Grain boundary energy, Acta Mater. 57 (13) (2009) 3694–3703, http://dx.doi.org/10.1016/j.actamat.2009.04.007.

[82] M. Yamaguchi, First-principles study on the grain boundary embrittlement of metals by solute segregation: Part I. Iron (Fe)-solute (B, C, P, and S) systems, Metall. Mater. Trans. A 42 (2) (2011) 319–329.

[83] J.I. Kim, J.H. Pak, K.-S. Park, J.H. Jang, D.-W. Suh, H.K.D.H. Bhadeshia, Segregation of phosphorus to ferrite grain boundaries during transformation in an Fe–P alloy, Int. J. Mater. Res. 105 (12) (2014) 1166–1172, http://dx.doi.org/10.3139/146.111129.

[84] T. Hajilou, I. Taji, F. Christien, S. He, D. Scheiber, W. Ecker, R. Pippan, V.I. Razumovskiy, A. Barnoush, Hydrogen-enhanced intergranular failure of sulfur-doped nickel grain boundary: In situ electrochemical micro-cantilever bending vs. DFT, Mater. Sci. Eng. A 794 (2020) 139967, http://dx.doi.org/10.1016/j.msea.2020.139967.

[85] R.Y. Rohling, I.C. Tranca, E.J.M. Hensen, E.A. Pidko, Correlations between density-based bond orders and orbital-based bond energies for chemical bonding analysis, J. Phys. Chem. C 123 (5) (2019) 2843–2854, http://dx.doi.org/10.1021/acs.jpcc.8b08934.